Monthly Notices
of the
ROYAL ASTRONOMICAL SOCIETY

Mon. Not. R. Astron. Soc. **424,** 3050–3080 (2012) doi:10.1111/j.1365-2966.2012.21453.x

The JCMT Nearby Galaxies Legacy Survey – VIII. CO data and the $L_{CO(3-2)}$–L_{FIR} correlation in the SINGS sample

C. D. Wilson,[1⋆] B. E. Warren,[1,2] F. P. Israel,[3] S. Serjeant,[4] D. Attewell,[1] G. J. Bendo,[5] H. M. Butner,[6] P. Chanial,[7] D. L. Clements,[8] J. Golding,[1] V. Heesen,[9] J. Irwin,[10] J. Leech,[11] H. E. Matthews,[12] S. Mühle,[13] A. M. J. Mortier,[14] G. Petitpas,[15] J. R. Sánchez-Gallego,[16,17] E. Sinukoff,[1] K. Shorten,[1] B. K. Tan,[11] R. P. J. Tilanus,[18,19] A. Usero,[20] M. Vaccari,[21,22] T. Wiegert,[23] M. Zhu,[24] D. M. Alexander,[25] P. Alexander,[26,27] M. Azimlu,[15,28] P. Barmby,[28] R. Brar,[10] C. Bridge,[29] E. Brinks,[9] S. Brooks,[1] K. Coppin,[30] S. Côté,[31] P. Côté,[31] S. Courteau,[10] J. Davies,[32] S. Eales,[32] M. Fich,[33] M. Hudson,[33] D. H. Hughes,[34] R. J. Ivison,[35,36] J. H. Knapen,[16,17] M. Page,[8] T. J. Parkin,[1] D. Rigopoulou,[11,37] E. Rosolowsky,[38] E. R. Seaquist,[39] K. Spekkens,[40] N. Tanvir,[41] J. M. van der Hulst,[42] P. van der Werf,[3] C. Vlahakis,[43] T. M. Webb,[30] B. Weferling[18] and G. J. White[4,38]

[1]*Department of Physics and Astronomy, McMaster University, Hamilton, Ontario L8S 4M1, Canada*
[2]*International Centre for Radio Astronomy Research, M468, University of Western Australia, 35 Stirling Hwy, Crawley, WA 6009, Australia*
[3]*Sterrewacht Leiden, Leiden University, PO Box 9513, 2300 RA Leiden, the Netherlands*
[4]*Department of Physics and Astronomy, The Open University, Milton Keynes MK7 6AA*
[5]*UK ALMA Regional Centre Node, Jodrell Bank Centre for Astrophysics, School of Physics and Astronomy, University of Manchester, Oxford Road, Manchester M13 9PL*
[6]*Department of Physics and Astronomy, James Madison University, MSC 4502-901 Carrier Drive, Harrisonburg, VA 22807, USA*
[7]*Laboratoire AIM-Paris-Saclay, CEA/DSM/Irfu, CNRS, Université Paris Diderot, CE-Saclay, pt courrier 131, F-91191 Gif-sur-Yvette, France*
[8]*Astrophysics Group, Imperial College, Blackett Laboratory, Prince Consort Road, London SW7 2AZ*
[9]*Centre for Astrophysics Research, University of Hertfordshire, College Lane, Hatfield AL10 9AB*
[10]*Department of Physics, Engineering Physics and Astronomy, Queen's University, Kingston, Ontario K7L 3N6, Canada*
[11]*Astrophysics, Oxford University, Keble Road, Oxford OX1 3RH*
[12]*National Research Council Canada, Herzberg Institute of Astrophysics, DRAO, PO Box 248, White Lake Road, Penticton, BC V2A 69J, Canada*
[13]*Joint Institute for VLBI in Europe, Postbus 2, 7990 AA Dwingeloo, the Netherlands*
[14]*Scottish Universities Physics Alliance, Institute for Astronomy, University of Edinburgh, Royal Observatory, Blackford Hill, Edinburgh EH9 3HJ*
[15]*Harvard–Smithsonian Center for Astrophysics, 60 Garden Street, Cambridge, MA 02138, USA*
[16]*Instituto de Astrofísica de Canarias, E-38205 La Laguna, Tenerife, Spain*
[17]*Departamento de Astrofísica, Universidad de La Laguna, E-38200 La Laguna, Tenerife, Spain*
[18]*Joint Astronomy Centre, 660 N. A'ohoku Pl., University Park, Hilo, HI 96720, USA*
[19]*Netherlands Organisation for Scientific Research, Laan van Nieuw Oost-Indie 300, NL-2509 AC The Hague, the Netherlands*
[20]*Observatorio de Madrid, OAN, Alfonso XII, 3, E-28014 Madrid, Spain*
[21]*Dipartimento di Astronomia, Universitá di Padova, Vicolo dell'Osservatorio 5, 35122 Padua, Italy*
[22]*Astrophysics Group, Physics Department, University of the Western Cape, Private Bag X17, 7535 Bellville, Cape Town, South Africa*
[23]*Department of Physics and Astronomy, University of Manitoba, Winnipeg, Manitoba R3T 2N2, Canada*
[24]*National Astronomical Observatories, Chinese Academy of Sciences 20A Datun Road, Chaoyang District, Beijing 100012, China*
[25]*Department of Physics, Durham University, Durham DH1 3LE*
[26]*Astrophysics Group, Cavendish Laboratory, 19 J. J. Thomson Avenue, Cambridge CB3 0HE*
[27]*Kavli Institute for Cosmology Cambridge, Madingley Road, Cambridge CB3 0HA*
[28]*Department of Physics and Astronomy, University of Western Ontario 1151 Richmond St., London, ON N6A 3K7, Canada*
[29]*California Institute of Technology, 1200 E. California Blvd., Pasadena, CA 91125, USA*
[30]*Department of Physics, McGill University, 3600 rue University, Montreal, QC H2A 2T8, Canada*
[31]*Herzberg Institute of Astrophysics, National Research Council of Canada, Victoria, BC V9E 2E7, Canada*
[32]*School of Physics and Astronomy, Cardiff University, Queens Buildings, The Parade, Cardiff CF24 3AA*
[33]*Department of Physics and Astronomy, University of Waterloo, Waterloo, Ontario N2L 3G1, Canada*
[34]*Instituto Nacional de Astrofisica, Optica y Electronica (INAOE), Aptdo. Postal 51 y 216, 72000 Puebla, Pue., Mexico*

⋆E-mail: wilson@physics.mcmaster.ca

[35] *UK Astronomy Technology Centre, Royal Observatory, Blackford Hill, Edinburgh EH9 3HJ*
[36] *Institute for Astronomy, University of Edinburgh, Royal Observatory, Blackford Hill, Edinburgh EH9 3HJ*
[37] *RALSpace, The Rutherford Appleton Laboratory, Chilton, Didcot OX11 0NL*
[38] *University of British Columbia, Okanagan Campus, 3333 University Way, Kelowna, BC V1V 1V7, Canada*
[39] *Department of Astronomy and Astrophysics, University of Toronto, 50 St. George Street, Toronto, ON M5S 3H4, Canada*
[40] *Department of Physics, Royal Military College of Canada, PO Box 17000, Station Forces, Kingston, ON K7K 7B4, Canada*
[41] *Department of Physics and Astronomy, University of Leicester, University Road, Leicester, LE1 7RH*
[42] *Kapteyn Astronomical Institute, University of Groningen, PO Box 800, 9700 AV Groningen, the Netherlands*
[43] *Joint ALMA Office, Alonso de Cordova 3107, Vitacura, Santiago, Chile*

Accepted 2012 June 7. Received 2012 May 23; in original form 2012 February 6

ABSTRACT

The James Clerk Maxwell Telescope Nearby Galaxies Legacy Survey (NGLS) comprises an H I-selected sample of 155 galaxies spanning all morphological types with distances less than 25 Mpc. We describe the scientific goals of the survey, the sample selection and the observing strategy. We also present an atlas and analysis of the CO $J = 3-2$ maps for the 47 galaxies in the NGLS which are also part of the *Spitzer* Infrared Nearby Galaxies Survey. We find a wide range of molecular gas mass fractions in the galaxies in this sample and explore the correlation of the far-infrared luminosity, which traces star formation, with the CO luminosity, which traces the molecular gas mass. By comparing the NGLS data with merging galaxies at low and high redshift, which have also been observed in the CO $J = 3-2$ line, we show that the correlation of far-infrared and CO luminosity shows a significant trend with luminosity. This trend is consistent with a molecular gas depletion time which is more than an order of magnitude faster in the merger galaxies than in nearby normal galaxies. We also find a strong correlation of the $L_{FIR}/L_{CO(3-2)}$ ratio with the atomic-to-molecular gas mass ratio. This correlation suggests that some of the far-infrared emission originates from dust associated with atomic gas and that its contribution is particularly important in galaxies where most of the gas is in the atomic phase.

Key words: stars: formation – ISM: molecules – galaxies: ISM – galaxies: kinematics and dynamics – galaxies: spiral.

1 INTRODUCTION

Star formation is one of the most important processes driving the evolution of galaxies. The presence or absence of significant star formation is one of the key characteristics which distinguish spiral and elliptical galaxies. The intense bursts of star formation triggered by galaxy interactions and mergers produce some of the most luminous galaxies in the local Universe (Sanders & Mirabel 1996). At high redshift, many galaxies are seen to be forming stars at rates which far exceed those of all but the most extreme local mergers (Tacconi et al. 2008, 2009). Since stars form from gas, specifically from molecular gas, understanding the properties of the interstellar medium (ISM) is critical to understanding the rate and regulation of star formation in galaxies (Bigiel et al. 2008; Leroy et al. 2008).

At the most basic level, the amount of gas in a galaxy is an important constraint on the amount of star formation the galaxy can sustain (Kennicutt 1989; Kennicutt et al. 2007; Bigiel et al. 2008; Leroy et al. 2008). Recent studies have shown that it is the amount of molecular gas that is most important, rather than the total gas content (Bigiel et al. 2008, 2011; Leroy et al. 2008). This picture is consistent with Galactic studies which show that stars form exclusively in molecular clouds, and most commonly in the densest regions of those clouds (Lada, Bally & Stark 1991a; Lada et al. 1991b; Arzoumanian et al. 2011). This suggests that the properties of the molecular gas, in particular its average density and perhaps the fraction of gas above a critical density on subparsec scales, are likely to affect the resulting star formation. Star formation in turn can affect the properties of the dense gas, by increasing its temperature (Wilson, Walker & Thornley 1997; Meier et al. 2001; Tosaki et al. 2007) and perhaps by triggering a subsequent generation of stars (Zavagno et al. 2010). Unusual environments are also likely to affect both the gas properties and the star formation process. High shear in galactic bars, harassment in a dense galaxy cluster, and galaxy mergers and interactions have the potential to either dampen or enhance the star formation process. The wide range of environmental processes at work, both on galactic and extragalactic scales, implies that large samples of galaxies are required to tease out the most important effects, while high resolution is required to isolate individual star-forming regions, separate arm from inter-arm regions and resolve galactic bars.

There have been a number of large surveys of the atomic gas content of nearby galaxies, of which some of the most recent include The H I Nearby Galaxy Survey (THINGS; Walter et al. 2008), the Arecibo Legacy Fast ALFA (ALFALFA) survey (Giovanelli et al. 2005) and the VLA Imaging of Virgo Spirals in Atomic Gas (VIVA) survey (Chung et al. 2009). However, only the 34 galaxies in the

THINGS and the 53 galaxies in the VIVA sample have sufficient spatial resolution to probe scales of 1 kpc and below. Compared to the H I 21-cm line, the CO lines used to trace molecular gas are relatively more difficult to observe due to their shorter wavelengths and the smaller field of view of millimetre-wave radio telescopes equipped with single pixel detectors. As a result, most CO extragalactic surveys have sampled a relatively small region at the centre of each galaxy (Braine et al. 1993; Young et al. 1995; Dumke et al. 2001; Helfer et al. 2003). Two recent surveys (Kuno et al. 2007; Leroy et al. 2009) have used array receivers to observe large unbiased regions, although still in relatively small (18 and 40) samples of galaxies. Finally, dust continuum observations in the submillimetre to far-infrared present an alternative method of tracing the molecular gas that requires a mostly independent set of physical parameters, such as dust emissivity, gas-to-dust mass ratio and the atomic gas mass (Thronson 1988; Israel 1997; Eales et al. 2010; Leroy et al. 2011). Two large surveys have been made at 850 μm, one of an *Infrared Astronomical Satellite* (*IRAS*) selected sample (Dunne et al. 2000) and one of an optically selected sample (Vlahakis, Dunne & Eales 2005). The galaxies selected for these samples were relatively distant (>25 Mpc) and thus primarily global measurements of the dust luminosity were obtained. The Herschel Reference Survey (Boselli et al. 2010) is observing 323 galaxies with distances between 15 and 25 Mpc at 250, 350 and 500 μm and has significant overlap with the sample presented here. Other Herschel surveys which overlap with the Nearby Galaxies Legacy Survey (NGLS) sample include the Key Insights on Nearby Galaxies: A Far-Infrared Survey with Herschel (Kennicutt et al. 2011) and the Herschel Virgo Cluster Survey (Davies et al. 2010). Using the dust continuum to measure the star-forming gas is a promising avenue to explore, especially since this method is one that can, in principle, be used for galaxies at higher redshifts.

Taking advantage of new instrumentation for both spectral line and continuum data on the James Clerk Maxwell Telescope (JCMT), we are carrying out the NGLS,[1] a large survey of 155 nearby galaxies using the CO $J = 3-2$ line and continuum observations at 850 and 450 μm. The survey is designed to address four broad scientific goals.

(i) *Physical properties of dust in galaxies.* The continuum data from this survey will probe a range of the dust spectral energy distribution (SED) that is critical to determining the total mass of dust as well as the relative proportion and physical properties of the different dust components (polycyclic aromatic hydrocarbons, very small grains, large grains). Most importantly, these long-wavelength data will trace any excess submillimetre emission that causes an upturn in the dust SED. The submillimetre excess could originate from: dust with <10 K temperatures (Galliano et al. 2003, 2005, 2011), very small grains with shallow dust emissivities that are not prominent in the dust SED between 60 and 500 μm (Lisenfeld et al. 2002; Zhu et al. 2009), large dust grains with enhanced dust emissivities at >850 μm (Bendo et al. 2006; O'Halloran et al. 2010), or spinning dust grains (Bot et al. 2010; Ade et al. 2011).

(ii) *Molecular gas properties and the gas-to-dust ratio.* Our high-resolution data will allow us to compare the radial profiles of the dust, H I and CO emission within our well-selected sample. The CO $J = 3-2$ line will effectively trace the warmer, denser molecular gas that is more directly involved in star formation (Iono et al. 2009). In comparison, the CO $J = 1-0$ line also traces more diffuse and low density gas (Wilson & Walker 1994; Rosolowsky et al. 2007). With observations of all three components of the ISM (molecular gas, atomic gas and dust), we will be able to determine accurate gas-to-dust mass ratios and provide constraints on the variation of the CO-to-H_2 conversion factor X_{CO} (Strong et al. 1988) by fitting the data (Thronson 1988; Braine et al. 1997; Israel 1997).

(iii) *The effect of galaxy morphology.* The larger-scale galaxy environment can play a significant role in the properties and structure of the dense ISM. For example, an increase in the density in the ISM in the centres of spiral galaxies has been attributed to an increased pressure (Helfer & Blitz 1993). Elliptical galaxies have relatively low column densities of gas and dust (Bregman et al. 1988; Knapp et al. 1989) combined with an intense radiation field dominated by older, low-mass stars and, in some cases, substantial X-ray haloes. Early-type galaxies also show more compact and symmetric distributions of dust at <70 μm compared to late-type galaxies (Bendo et al. 2007; Muñoz-Mateos et al. 2009). In spiral galaxies, dust and gas properties may differ between arm and inter-arm regions (Alton et al. 2002; Foyle et al. 2010), while the role of spiral arms in the star formation process is the subject of considerable debate (Elmegreen & Elmegreen 1986; Vogel, Kulkarni & Scoville 1988). With observations across the full range of galaxy morphologies and with sub-kiloparsec resolution, we will be able to study the effect of morphology on the molecular gas properties.

(iv) *The impact of unusual environments.* Metallicity has been shown to affect the structural properties of the ISM (Leroy et al. 2011). Lower self-shielding is expected to produce smaller regions of cold, dense gas that can be traced by CO emission with relatively larger and warmer photon-dominated regions (Madden et al. 1997, 2006). Galaxies residing in rich clusters can be affected by ram-pressure stripping (Lee, McCall & Richer 2003) and gravitational harassment (Moore, Lake & Katz 1998) which reduces their ISM content relative to field galaxies. The haloes of spiral galaxies can be populated with gas via superwinds or tidal interactions (Roussel et al. 2010) or even by relatively normal rates of star formation (Lee & Irwin 1997). With its galaxies spanning the full range of environment, from isolated galaxies to small groups to the dense environment of the Virgo cluster, the NGLS will be able to quantify the effect of environment on the molecular ISM in galaxies.

Most surveys of molecular gas in our own or other nearby galaxies have used the ground state CO $J = 1-0$ line as a tracer. The choice of the CO $J = 3-2$ line for the NGLS was driven by the available instrumentation at the JCMT. Compared to the CO $J = 1-0$ line (5.5 K above ground with a critical density of 1.1×10^3 cm^{-3}), the CO $J = 3-2$ line (33 K and 2.1×10^4 cm^{-3}) traces relatively warmer and denser gas. (Since both lines are usually optically thick, the effective critical density is likely reduced by a factor of 10 or more.) There is growing evidence that the CO $J = 3-2$ emission correlates more tightly with the star formation rate or star formation efficiency than does the CO $J = 1-0$ line (Muraoka et al. 2007; Wilson et al. 2009). Komugi et al. (2007) showed that the CO $J = 3-2$ emission correlates linearly with star formation rate derived from extinction-corrected Hα emission and that the correlation was tighter with the $J = 3-2$ line than with the $J = 1-0$ line. Similarly, Iono et al. (2009) showed that the CO $J = 3-2$ emission correlates nearly linearly with the far-infrared luminosity for a sample of local luminous infrared galaxies and high-redshift submillimetre galaxies. Thus, it appears that the CO $J = 3-2$ emission is preferentially tracing the molecular gas associated directly with star formation, such as high-density gas

[1] http://www.jach.hawaii.edu/JCMT/surveys/

that is forming stars or warm gas heated by star formation, rather than the total molecular gas content of a galaxy.

In this paper, we describe the NGLS sample selection, the CO $J = 3-2$ observations and data reduction, and the planned observing strategy for continuum 450 and 850 μm observations (Section 2). In Section 3, we present the CO $J = 3-2$ integrated intensity images, as well as maps of the velocity field and velocity dispersion for those galaxies with sufficiently strong signal. In Section 4, we examine the molecular and atomic gas masses for the *Spitzer* Infrared Nearby Galaxies Survey (SINGS) sample (Kennicutt et al. 2003) and compare the CO $J = 3-2$ luminosity with the far-infrared luminosity for both the galaxies in the SINGS sample, local luminous and ultraluminous infrared galaxies, and high-redshift quasars and submillimetre galaxies which have also been observed in the CO $J = 3-2$ transition (Iono et al. 2009). We give our conclusions in Section 5. Previous papers in this series have examined individual or small samples of galaxies (Wilson et al. 2009, 2011; Bendo et al. 2010a; Warren et al. 2010; Irwin et al. 2011; Sanchez-Gallego et al. 2011). Future papers will exploit the spatially resolved nature of these data by examining the CO line ratios and excitation (Rosolowsky et al., in preparation) and the gas depletion times (Sinukoff et al., in preparation).

2 OBSERVATIONS AND DATA PROCESSING

2.1 Sample selection

The galaxies in the NGLS are an H I-flux-selected sample. This selection method was chosen to avoid biasing the survey towards galaxies with higher star formation rates, as might be the case for far-infrared or blue magnitude selection criteria, while still targeting galaxies with a significant ISM, as might not be the case for a purely mass-selected sample, e.g. Boselli et al. (2010). Our sample should also not be unduly biased by dust content being either particularly hot or cold, and should be reasonably representative of the local submillimetre Universe. H I emission typically extends to much a larger radius than CO or stellar emission, so that our sample may include galaxies that are H I-rich but H_2-poor.

To obtain good spatial resolution while still being able to obtain sensitive maps in a reasonable period of time, the galaxies were selected to have distances between 2 and 25 Mpc. This distance limit excludes galaxies in the Local Group but does include galaxies in the Virgo cluster, which allows us to test the effect of cluster environment on the dense ISM. We used the HyperLeda[2] data base (Paturel et al. 2003) in 2005 February to extract all non-Virgo galaxies (see below) with H I fluxes >3.3 Jy km s^{-1} and Virgo-corrected galactocentric velocities $v < 1875$ km s^{-1}. Out to these limits, the HyperLeda data base is essentially complete. We removed galaxies with declinations below -25°; we further removed galaxies with Galactic latitudes between -25° and 25° to minimize the impact of Galactic cirrus in complementary data from *Spitzer* and *Herschel*. Virgo cluster member galaxies were selected to be galaxies within an $8^\circ \times 16^\circ$ ellipse centred on M87 (RA $= 12^h.4$, Dec. $= 12^\circ.4$) and with velocities between 500 and 2500 km s^{-1}, e.g. Davies et al. (2004); all Virgo galaxies with an H I flux entry were included in this initial selection. These selection criteria gave us a sample of 1002 field galaxies and 148 Virgo cluster galaxies.

Since we estimated that at least 1500 h of telescope time would be required to observe this complete sample of 1150 galaxies, we needed to apply further selection criteria. We first selected all the SINGS galaxies (Kennicutt et al. 2003) that met our declination and Galactic latitude criteria; the wealth of complementary data available on these galaxies from the SINGS and other surveys (Walter et al. 2008) make them natural targets. 47 SINGS galaxies met our criteria (Tables 1 and 2). Two SINGS galaxies, NGC 5194 (M51) and NGC 4789A (DDO 154), were observed in separate programmes and were not re-observed as part of our survey; we present maps made from those data in this paper.

We then estimated the minimum size of the field and Virgo cluster samples that would allow us to achieve the scientific goals of this study. For statistical studies of galaxy properties, we want to divide the galaxies into four morphological bins (E/S0, early-type spirals, late-type spirals and irregulars). In addition, we want to compare the properties of galaxies in the Virgo cluster with those in the field. We estimated that 18 galaxies per bin were required to obtain good statistics on the average properties of each bin, or 144 galaxies total. However, since our sample only contains 148 Virgo galaxies, we compromised on nine galaxies per bin in Virgo and 18 per bin in the field, giving a sample size of 108 galaxies. In addition, we limited the field and Virgo samples to galaxies with $D_{25} < 5$ arcmin so that we could use the jiggle-map mode with HARP-B (Buckle et al. 2009) and still map the inner quarter of each galaxy.

To select the final sample, the field and Virgo lists were each divided into the four morphological bins described above using the numerical Hubble stage, T (E/S0: $T \leq 0.5$; early-type spirals: $0.5 < T \leq 4.5$; late-type spirals: $4.5 < T \leq 9.5$; irregulars: $T > 9.5$). For the field samples, we first applied an H I flux cut-off of 6.3 Jy km s^{-1} and then randomly selected 18 galaxies in each of the four morphological bins (for the elliptical galaxies, there were precisely 18 galaxies above this cut-off). The smaller Virgo sample meant that we could only use this same process for the late-type spiral bin. The brightest nine in each category of E/S0 ($\geq$2.1 Jy km s^{-1}), Irr ($\geq$4.1 Jy km s^{-1}) and early-type spiral galaxies ($\geq$6.2 Jy km s^{-1}) from Virgo were included, in addition to a random selection of nine late-type spirals with H I fluxes brighter than 6.3 Jy km s^{-1}. The final field and Virgo source lists are given in Tables A1 and A2 in Appendix A.

2.2 CO $J = 3-2$ observations and data processing

CO $J = 3-2$ observations for all galaxies were obtained on the JCMT between 2007 November and 2009 November. The angular resolution of the JCMT at this frequency is 14.5 arcsec, which corresponds to a linear resolution ranging from 0.2 to 1.2 kpc for the galaxies in our sample. The 30 large ($D_{25} > 4$ arcmin) SINGS galaxies in the NGLS were observed in raster map mode, while the smaller galaxies were observed in jiggle-map mode (Buckle et al. 2009). All galaxies were mapped over a rectangular area corresponding to $D_{25}/2$ on a side (with raster maps oriented with the position angle of the galaxy's semimajor axis), with a 1σ sensitivity of better than 19 mK (T_A^*) (32 mK T_{MB} for $\eta_{MB} = 0.6$) at a spectral resolution of 20 km s^{-1}. We used the 16 pixel array receiver HARP-B (Buckle et al. 2009) with the Auto-Correlation Spectral Imaging System (ACSIS) correlator configured to have a bandwidth of 1 GHz and a resolution of 0.488 MHz (0.43 km s^{-1} at the frequency of the CO $J = 3-2$ transition). The total time allocated to the CO $J = 3-2$ portion of the NGLS, including pointing and calibration observations, was 256 h.

Calibration was checked each night by observing one or more of a set of six calibrator sources in the ^{12}CO $J = 3-2$ transition. The calibration sources used were W75N, CRL 618, IRC+10216, NGC

[2] http://leda.univ-lyon1.fr

Table 1. Large ($D_{25} > 4$ arcmin) galaxies from the SINGS sample.

Name	α(J2000.0)[a] (h:m:s)	δ(J2000.0)[a] (°:′:″)	$D_{25,\mathrm{maj}}/2$[b] (arcmin)	$D_{25,\mathrm{min}}/2$[b] (arcmin)	PA (°)	V_{hel}[c] (km s^{-1})
NGC 0024	00:9:56.6	−24:57:47	3.1	0.8	46	563
NGC 0628[d]	01:36:41.8	+15:47:00	5.2	4.8	25	648
NGC 0925[d]	02:27:17.0	+33:34:44	5.6	3.2	102	540
NGC 2403[d]	07:36:50.7	+65:36:10	11.7	6.2	127	121
UGC 04305	08:19:03.9	+70:43:09	4.2	3.1	15	158
NGC 2841[d]	09:22:02.5	+50:58:36	3.8	1.8	147	641
NGC 2976[d]	09:47:15.5	+67:55:03	2.9	1.5	143	22
NGC 3031[d]	09:55:33.1	+69:03:56	11.2	5.7	157	−48
NGC 3034[d]	09:55:52.4	+69:40:47	5.2	2.2	65	254
NGC 3184[d]	10:18:17.0	+41:25:28	4.0	3.8	135	574
NGC 3198[d]	10:19:55.0	+45:32:59	3.9	1.3	35	666
IC 2574[d]	10:28:23.5	+68:24:44	6.7	3.2	50	28
NGC 3351[d]	10:43:57.8	+11:42:13	3.8	2.2	13	768
NGC 3521[d]	11:05:48.9	−00:02:06	5.4	2.7	163	778
NGC 3627[d]	11:20:14.9	+12:59:30	4.4	2.0	173	697
NGC 3938[d]	11:52:49.3	+44:07:17	2.5	2.4	0	829
NGC 4236	12:16:42.0	+69:27:46	11.4	3.6	162	10
NGC 4254[d]	12:18:49.6	+14:25:00	2.7	2.3	0	2412
NGC 4321[d]	12:22:54.9	+15:49:21	3.8	3.1	30	1599
NGC 4450	12:28:29.7	+17:05:06	2.6	1.9	175	1905
NGC 4559	12:35:57.7	+27:57:36	6.0	2.1	150	827
NGC 4569[d]	12:36:50.0	+13:09:46	5.2	2.3	23	−179
NGC 4579[d]	12:37:44.0	+11:49:07	2.8	2.2	95	1540
NGC 4594	12:39:59.3	−11:37:22	4.2	2.0	90	1088
NGC 4631[d]	12:42:07.7	+32:32:34	7.4	1.3	86	640
NGC 4725	12:50:26.7	+25:30:03	5.5	3.7	35	1188
NGC 4736	12:50:53.1	+41:07:12	6.3	5.5	105	295
NGC 4826	12:56:43.9	+21:41:00	5.4	2.6	115	390
NGC 5033[d]	13:13:27.6	+36:35:38	5.1	1.9	170	873
NGC 5055[d]	13:15:49.4	+42:01:46	6.6	4.0	105	495
NGC 5194[d]	13:29:52.4	+47:11:41	4.9	3.4	163	452

[a]From RC3 (de Vaucouleurs et al. 1991).
[b]From Buta, Corwin & Odewahn (2007).
[c]Systemic velocity from the H I line (heliocentric).
[d]Member of high-priority SINGS subset for SCUBA-2 observations.

Table 2. Small ($D_{25} < 4$ arcmin) galaxies from the SINGS sample.

Name	α(J2000.0)[a] (h:m:s)	δ(J2000.0)[a] (°:′:″)	V_{hel}[b] (km s^{-1})	Alternative name
NGC 0337	00:59:50.1	−07:34:41	1664	–
NGC 0584	01:31:20.8	−06:52:05	1861	–
NGC 0855	02:14:03.6	+27:52:38	583	–
PGC 023521	08:23:55.0	+71:01:57	113	M81DwA
UGC 05139	09:40:32.3	+71:10:56	137	HoI
NGC 3049	09:54:49.7	+09:16:18	1458	–
UGC 05336	09:57:32.1	+69:02:46	48	HoIX
UGC 05423	10:05:30.4	+70:21:54	344	M81DwB
NGC 3190	10:18:05.3	+21:49:58	1306	–
NGC 3265	10:31:06.8	+28:47:47	1410	–
UGC 05720	10:32:32.0	+54:24:04	1456	Mrk33
NGC 3773	11:38:13.0	+12:06:43	1002	–
NGC 4625	12:41:52.7	+41:16:26	590	–
NGC 4789A	12:54:05.5	+27:08:55	374	DDO154
UGC 08201	13:06:24.9	+67:42:25	34	DDO165
NGC 5474	14:05:01.6	+53:39:45	240	–

[a]From RC3 (de Vaucouleurs et al. 1991).
[b]Systemic velocity from the H I line (heliocentric).

2071IR, CRL 2688 and IRAS 17293−2422. The peak intensities of the calibrator spectra agreed to within ±8 per cent, while the integrated intensities agreed to within ±13 per cent from 2007 November to 2008 July and to ±9 per cent from 2008 August onwards. We adopt 10 per cent as the internal calibration uncertainty on the NGLS. Pointing was checked before starting a new source, and every 1–2 h (more frequently near sunrise and sunset). Any scan where the pointing offset that was measured after the scan differed by more than 4 arcsec from the pointing measured at the start of the scan was rejected in the final data analysis. Less than 5 per cent of the data were rejected because of large pointing changes. The rms of the pointing measurements on a given night was typically better than 2 arcsec.

Two sources in the NGLS, NGC 5055 and NGC 337, were observed during science verification runs in 2007 May and 2007 July. For these observing runs, the strength of the spectral line calibrators was only 85 per cent of the expected values and so the data for these two galaxies have been rescaled by a factor of 1.18 to bring them on to the same calibration scale as the rest of the survey. NGC 4789A (DDO 154) was observed as part of a separate programme (M07AC14, PI B. Warren), as was NGC 5194 (M51) (M06AN05, PI R. Tilanus). For both these galaxies, the integration time per point in the map is longer than that of a typical NGLS observation.

Details of the reduction of the raster map data are given in the appendix in Warren et al. (2010) and so we discuss only the jiggle-map processing in detail here. The individual raw data files were flagged to remove data from any of the 16 individual receptors with bad baselines and then the scans were combined into a data cube using the 'nearest' weighting function to determine the contribution of individual receptors to each pixel in the final map. This weighting function causes each measurement from a raw data file to contribute to only a single pixel in the final cube. The pixel size in the maps is 7.5 arcsec. We fitted and subtracted a first-order baseline from the data cube while excluding the central 400 km s^{-1} region from the baseline fit.

We used the CLUMPFIND algorithm (Williams et al. 1994) implemented as part of the Clump Identification and Analysis Package (CUPID[3]) (Berry et al. 2007) task FINDCLUMPS to identify regions with emission above a specified signal-to-noise ratio. The algorithm measures the mean noise in the data cube as part of the processing step. However, the sensitivity of each of the 16 individual receptors in the HARP-B array varies quite significantly. In addition, a portion of the data was obtained when four of the receptors were inoperative and a rotation of the *K*-mirror between two observations was used to obtain a complete map of the desired area. As a result, the noise in a final data cube can vary quite significantly from region to region in a jiggle map. Thus, the mean noise that FINDCLUMPS measures will under- or overestimate the noise in different regions of the cube.

To mitigate the effect of this noise variation, we calculated an image of the noise in the map by averaging the noise in the line-free regions at the end of the spectrum. We then divided the cube by this noise image to produce a cube which was now in units of signal-to-noise ratio rather than Kelvins. This data cube was then boxcar smoothed by three pixels and 25 velocity channels. We then applied the FINDCLUMPS algorithm to this signal-to-noise ratio cube to identify regions with emission with signal-to-noise ratio greater than 2σ, 2.5σ or 3σ. In all cases, the spacing between contour levels (the ΔT parameter) was set to 2σ. The mask of regions of real emission produced by FINDCLUMPS was then applied to the original, unsmoothed data cube and this masked cube was then collapsed in velocity to produce moment maps. For the raster maps, we produced masks with signal-to-noise ratio cut-offs of 2σ, 2.5σ and 3σ.

[3] CUPIDis part of the STARLINK (Currie et al. 2008) software package, which is available for download from http://starlink.jach.hawaii.edu.

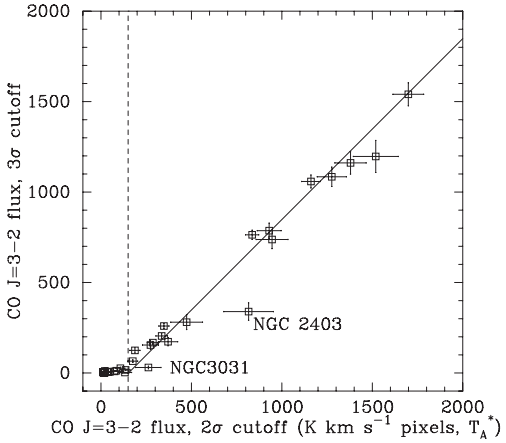

Figure 1. CO $J = 3-2$ flux for galaxies in the NGLS compared for a 2σ cut-off versus a 3σ cut-off in making the moment maps. The solid line represents 2σ flux $= 152 + 3\sigma$ flux (see text). NGC 3034 (M82) is much brighter than all other galaxies and is not included in this plot; its flux offset is consistent with the rest of the sample. Galaxies to the left of the vertical dashed line were not included in calculating the average offset (see text).

The zeroth moment map measures the integrated intensity in the data cube, $\int T \mathrm{d}v = \sum T_i \Delta v$, where Δv is the channel width and T_i is the temperature in an individual channel. To obtain the final integrated intensity map, the zeroth moment map needed to be multiplied by the noise map (to recover units of K km s^{-1}) and also to be divided by $\eta_{MB} = 0.6$ to convert to the T_{MB} temperature scale. For the zeroth moment maps, we use a noise cut-off of 2σ; we chose to use this cut-off after comparing the CO fluxes obtained with different noise cut-offs (Fig. 1). For bright galaxies with a flux greater than 150 K (T_A^*) km s^{-1} pixels, the data show that fluxes measured using a 2σ cut-off are systematically offset from fluxes measured with a 3σ cut-off, in the sense that the maps made with the 3σ cut-off underestimate the total flux. Two galaxies, NGC 2403 (Bendo et al. 2010a) and NGC 3031 (Sanchez-Gallego et al. 2011), have much larger offsets and were not included in deriving the average offset. These galaxies both have such low CO surface brightnesses such that an increase in the noise cut-off causes large areas of the galaxy to be masked out and thus has a large impact on the total flux that is measured.

The first moment map measures the mean velocity of the emission $\overline{v} = \sum T_i v_i / \sum T_i$, where v_i is the velocity of a given velocity channel. The mean velocity calculated in this way can be rather sensitive to noise spikes, and so we used a higher signal-to-noise ratio threshold of 2.5σ in calculating the velocity field maps.

The second moment maps measure the velocity dispersion, σ_v, for each pixel in the image using

$$\sigma_v = \sum T_i (v_i - \overline{v})^2 / \sum T_i. \quad (1)$$

This method of calculating the velocity dispersion differs from those used in previous extragalactic CO studies such as Combes & Becquaert (1997), which typically fit Gaussian profiles to the CO lines. However, in the limit of Gaussian lines with a high signal-to-noise ratio, the values from the second moment maps should agree with the results from fitting a Gaussian directly to the line profiles. Note that for a Gaussian line profile, σ_v is equal to the full-width at half-maximum of the line divided by a factor of 2.355.

The second moment maps were calculated using a signal-to-noise ratio threshold of 2.5σ. A more detailed discussion of the possible systematics in second moment maps is given in Wilson et al. (2011).

CO $J = 3-2$ images for the SINGS sample are shown in Appendix C. Images for the Virgo and field samples will be presented in a future paper (Golding et al., in preparation). The reduced images, noise maps and spectral cubes are available via the survey website[4] and will eventually be made available via the Canadian Astronomical Data Centre (CADC). We note that some of the images show residual noise effects, particularly around the outer edges of the map (see NGC 4736 and NGC 5033 for particularly obvious examples). These artefacts are generally due to the increasing noise level in the data cubes towards the edges of the map, which due to the scanning technique do not have as long an integration time and are not sampled by as many of the individual HARP detectors. Anyone interested in the reality of a particular faint feature is encouraged to consult the images and noise maps available on the survey website.

2.3 Future SCUBA-2 observations

The Submillimetre Common-User Bolometer Array-2 (SCUBA-2; Holland et al. 2006) is a large-format bolometer camera for the JCMT that is designed to produce simultaneous continuum images at 450 and 850 μm. The camera consists of four 32×24 transition-edge sensor arrays for each of the two wavelengths and has a total field of view of $\sim 7 \times 7\,\mathrm{arcmin}^2$. The SCUBA-2 portion of the NGLS began in 2011 December with a period of science verification observations for the legacy surveys. In this section, we briefly describe our planned observing strategy with SCUBA-2.

The ultimate goal of the survey is to map all the galaxies in the NGLS with SCUBA-2 out to D_{25} to a 1σ limit of 1.7 mJy at 850 μm; this sensitivity limit includes both instrumental noise and confusion noise from the high-redshift extragalactic background. Good 450 μm data provide improved spatial resolution and are critical to tracing the upturn of the dust SED that indicates the presence of very cold dust or a change in dust properties (see Section 1). With similar (simultaneous) integration times at both 450 and 850 μm, we estimate that the 450-μm sensitivity will be about a factor of 2 worse than at 850 μm for a given surface density of dust and smoothed to the same angular resolution.

To put these sensitivities in physical terms, we can convert to an equivalent mass surface density (gas plus dust) by using the formula given in Johnstone et al. (2000). Assuming $T_{\rm dust} = 20\,\mathrm{K}$, $\kappa_{850} = 0.0043\,\mathrm{cm}^2\,\mathrm{g}^{-1}$, and a circular beam with diameter 15 arcsec, a 4σ detection at 850 μm corresponds to an average visual extinction of $A_{\rm v} = 3$ mag, which corresponds to surface densities of 6×10^{21} $\mathrm{H\,cm^{-2}}$ or $45\,\mathrm{M_\odot\,pc^{-2}}$. For a galaxy at a distance of 10 Mpc, the equivalent mass sensitivity is $2 \times 10^7\,\mathrm{M_\odot}$, equal to a few massive giant molecular clouds within a 730-pc diameter region.

3 CO PROPERTIES

3.1 Measuring CO luminosities

For galaxies which were clearly detected, the CO $J = 3-2$ luminosity was measured directly from the moment 0 images made with a 2σ cut-off mask. We used apertures chosen by eye to capture all the emission from the galaxy while excluding the occasional noisy or doubtful emission towards the edges of the map. Thus, the CO luminosity is given by

$$L_{\rm CO(3-2)} = \sum I({\rm CO})_i \times (4.848 D_{\rm Mpc} \times L_{\rm pix})^2, \quad (2)$$

where $I(\mathrm{CO})_i$ is the CO intensity in an individual pixel of the map, $D_{\rm Mpc}$ is the distance to the galaxy in Mpc and $L_{\rm pix}$ is the size of an individual pixel in the map (7.5 arcsec for jiggle maps and 7.2761 arcsec for raster maps).

We calculated a map of the uncertainty in $I(\mathrm{CO})$ for each pixel, σ_i, as

$$\sigma_i = \sigma_{\rm chan} \sqrt{\Delta v_{\rm chan} \Delta v_{\rm line}} \sqrt{1 + \Delta v_{\rm line}/\Delta v_{\rm base}}, \quad (3)$$

where $\Delta v_{\rm chan}$ is the velocity width of a single channel, $\sigma_{\rm chan}$ is the standard deviation in K of the line-free channels, $\Delta v_{\rm line}$ is the velocity range used to measure the line, and $\Delta v_{\rm base}$ is the velocity range used to fit the baseline. Now, both the raster and the jiggle observing modes use a shared off position observed for a longer integration time than each of the individual on positions. Because the off position is shared across many pixels in the map, a simple combination of the noise for each pixel in the map will underestimate the true uncertainty. Assuming an on-source integration time per pixel of $t_{\rm on}$ and a corresponding integration time on the off position of $t_{\rm off}$, the uncertainty in the CO luminosity is given by

$$\sigma_{L(\rm CO)} = \sqrt{(1-a)\sum \sigma_i^2 + a\left(\sum \sigma_i\right)^2} \times (4.848 D_{\rm Mpc} \times L_{\rm pix})^2, \quad (4)$$

where $a = 1/(t_{\rm off}/t_{\rm on} + 1)$ (see Appendix B). For the jiggle-map mode, $t_{\rm off} = 4t_{\rm on}$ and so $a = 0.2$. For the raster maps, the ratio of $t_{\rm off}/t_{\rm on}$ varied with the size and dimensions of the map; we have estimated an average value of $a = 1.07$ for the rasters and have used this in the noise calculations for all the galaxies.

For galaxies without detections, we calculated an uncertainty map using equation (3) by adopting a line width of $100\,\mathrm{km\,s^{-1}}$ and then calculated $\sigma_{L(\rm CO)}$ using equation (4). For galaxies observed in jiggle-map mode, the velocity width for the baseline determination was always $400\,\mathrm{km\,s^{-1}}$. For the galaxies observed in raster mode, the actual region used to determine the baseline varied slightly from pixel to pixel as a result of weak emission appearing from place to place in the spectrum. For these galaxies, we used the actual region used for the baseline in calculating σ_i for each pixel.

Of the 31 large galaxies in the SINGS sample, 25 galaxies were detected for a detection rate of 77 per cent. Of the 16 smaller galaxies, only four galaxies (NGC3049, NGC 3773, NGC 4625 and UGC 05720) are detected at $>4\sigma$ in the integrated intensity maps. A fifth galaxy, NGC 3190, is marginally detected at the 3σ level. Thus, the detection rate for the small SINGS galaxies is 25 per cent, significantly lower than for the larger SINGS galaxies. These smaller SINGS galaxies tend to be physically smaller galaxies (often dwarf galaxies) and also have on average lower H I fluxes than their larger counterparts, both of which may impact the detection rate.

3.2 Comparison with other surveys and the global CO line ratio

Because the different CO lines have different excitation temperatures and critical densities (Section 1), comparing the emission from different CO lines can provide information on the physical conditions in the molecular gas. These different excitation conditions may also produce different radial distributions in the different CO lines. The HERA CO-Line Extragalactic Survey (HERACLES; Leroy et al. 2009) mapped 18 nearby galaxies in the CO $J = 2-1$ line. The large area covered per galaxy and excellent sensitivity make

[4] http://www.physics.mcmaster.ca/~wilson/www_xfer/NGLS/

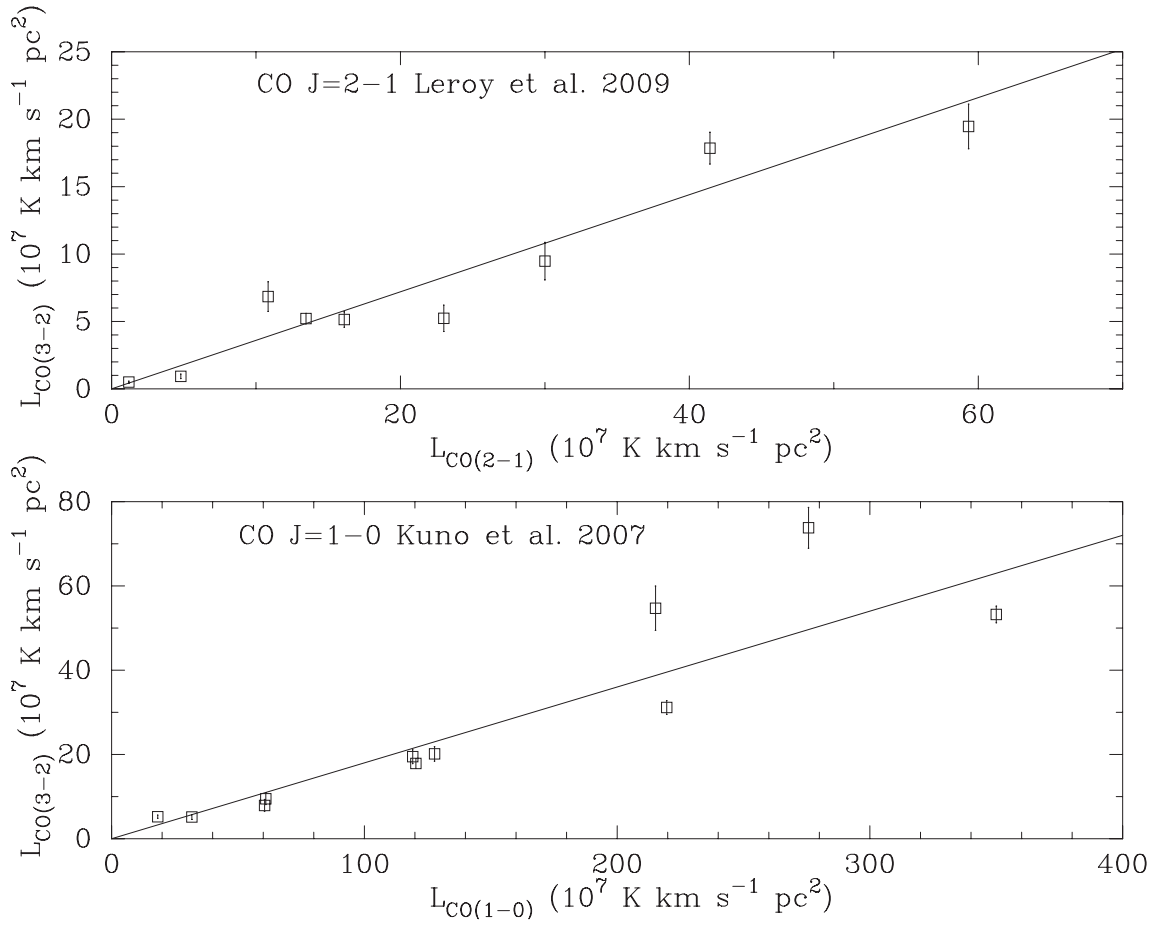

Figure 2. Top: $L_{CO(3-2)}$ versus $L_{CO(2-1)}$ for all galaxies detected in both the NGLS and the HERACLES surveys (Leroy et al. 2009). The HERACLES luminosities have been adjusted to use the distances adopted in this paper. Calibration uncertainties in the HERACLES data are estimated at 20 per cent (Leroy et al. 2009). The line shows the mean CO $J = 3{-}2/2{-}1$ ratio of 0.36 determined from the data points (see text). Bottom: $L_{CO(3-2)}$ versus $L_{CO(1-0)}$ for all galaxies detected in both the NGLS and the survey of Kuno et al. (2007). The CO $J = 1{-}0$ luminosities have been adjusted to use the distances adopted in this paper. The line shows the mean CO $J = 3{-}2/1{-}0$ ratio of 0.18 determined from the data points (see text).

the data from this survey an excellent comparison to the NGLS. Fig. 2 compares the CO luminosities for the nine galaxies that were detected in both surveys. (Three additional galaxies in common had only upper limits in both surveys, and NGC 2841 was detected by HERACLES but not by us.) The correlation between the two sets of global measurements is good, with a mean CO $J = 3{-}2/2{-}1$ line ratio of 0.36 ± 0.04 (where the quoted uncertainty is the standard deviation of the mean; the standard deviation is 0.13). Kuno et al. (2007) mapped 40 nearby galaxies in the CO $J = 1{-}0$ line, also covering a large area with good sensitivity, although the fact that the maps are somewhat undersampled may introduce some scatter. Fig. 2 compares the CO luminosities for the 11 galaxies that were detected in both surveys. The correlation between the two sets of measurements is again good, with a mean CO $J = 3{-}2/1{-}0$ line ratio of 0.18 ± 0.02 (standard deviation 0.06).

This average CO $J = 3{-}2/1{-}0$ line ratio is somewhat smaller than the line ratios (0.4–0.8) seen in individual giant molecular clouds in M33 (Wilson et al. 1997) and is at the low end of the range (0.2–1.9) measured in the central regions of galaxies (Mauersberger 1999; Mao et al. 2010). However, the sample of Mao et al. (2010) includes roughly 50 per cent Seyfert, low-ionization nuclear emission-line region (LINER), merging or OH megamaser galaxies which tend to show a higher than average line ratio. Not surprisingly, our average line ratio is also at the small end of the line ratios (0.1–1.9) measured for low-redshift luminous infrared galaxies (Leech et al. 2010; Papadopoulos et al. 2012). Note also that we have not attempted in either comparison to correct for differences in the fraction of the galaxy mapped in each survey. Given the differences in the processing techniques adopted between the three surveys, the small scatter in this relationship is a good indicator that both surveys are successfully measuring global CO luminosities in the low signal-to-noise ratio regime. A more detailed analysis of spatially resolved images of the CO line ratios by combining these various surveys with new ^{13}CO data will be presented in Rosolowsky et al. (in preparation).

4 COMPARISON WITH OTHER GLOBAL PROPERTIES

4.1 The molecular mass fraction in the interstellar medium

To examine the molecular gas mass fraction in the ISM of the SINGS galaxies in our sample, we have converted the CO $J = 3{-}2$ luminosities to molecular hydrogen mass adopting a CO-to-H_2 conversion factor of $X_{CO} = 2 \times 10^{20}$ cm^{-2} (K km s^{-1})$^{-1}$ (Strong et al. 1988). We have adopted a CO $J = 3{-}2/J = 1{-}0$ line ratio of 0.18, which is the mean value derived from our comparison with the Kuno et al. (2007) sample. With these assumptions, the molecular

hydrogen mass is given by

$$M_{\rm H_2} = 17.8(R_{31}/0.18)^{-1} L_{\rm CO(3-2)}, \quad (5)$$

where R_{31} is the CO $J = 3{-}2/J = 1{-}0$ line ratio, $M_{\rm H_2}$ is in $\rm M_\odot$, and $L_{\rm CO(3-2)}$ is in units of K km s^{-1} pc^2. We note that the mean value for the line ratio may not be appropriate for all galaxies; in particular, it may result in an overestimate of the H_2 mass for more luminous galaxies and an underestimate in less luminous galaxies. We also note that adopting a single value for the CO-to-H_2 conversion factor, $X_{\rm CO}$, will likely result in an underestimate of the molecular gas mass in galaxies or regions of galaxies where the metallicity is more than about a factor of 2 below solar (Wilson 1995; Arimoto, Sofuie & Tsujimot 1996; Bolatto et al. 2008). Finally, our adopted value of $X_{\rm CO}$ will likely result in an overestimate of the gas mass in the starburst galaxy M82, as lower values of $X_{\rm CO}$ are more appropriate in starburst and luminous infrared galaxies (Downes & Solomon 1998).

We have compiled H I fluxes from the literature for all of our sample. The preferred references were Walter et al. (2008) and Chung et al. (2009), with most of the remaining galaxies retrieved from the HyperLeda data base (Paturel et al. 2003). The H I flux for UGC 08201 is from Cannon et al. (2011), while the H I flux for NGC 3190 is taken from Martin (1998). All fluxes have been converted to H I masses using the distances in Table 3 and the equations given in Walter et al. (2008). Fig. 3 shows the H_2/H I mass fraction as a function of H I mass for all the SINGS galaxies. Of the galaxies with CO detections, 10 galaxies have H_2/H I mass fractions greater than 1, 9 galaxies of $0.5 < M_{\rm H_2}/M_{\rm H\,I} < 1$ and 10 galaxies have H_2/H I mass fractions less than 0.5. The 18 galaxies for which we have only CO upper limits span a similar range of atomic gas masses, although 78 per cent of these galaxies have H I masses less than 1.5×10^9 $\rm M_\odot$. On average, these galaxies have significantly lower molecular gas fractions than the detected galaxies.

The H_2/H I mass fractions shown here are on average somewhat larger than similar measurements for 14 galaxies given in Leroy et al. (2009). For the nine galaxies in common with our survey, the mass fraction given in Leroy et al. (2009) is a factor of $\sim$1.5 times smaller than the values for the same galaxies given in Table 3. The primary reason for this difference appears to be the CO line ratio. Leroy et al. (2009) adopt a CO $J = 2{-}1/J = 1{-}0$ line ratio of 0.8 measured from comparing the peak line temperatures with several surveys, including that of Kuno et al. (2007). On the other hand, comparing the global CO luminosities for five galaxies in common between these two surveys gives an average CO $J = 2{-}1/J = 1{-}0$ ratio of 0.52 ± 0.06. If we rescale the mass fractions given in Leroy et al. (2009) to this lower line ratio, the average agreement between their mass fractions and our values is good.

This comparison illustrates the importance of using the appropriate value of the CO line ratio when observing galaxies in the higher CO transitions. It is likely too simplistic to calculate gas masses using a single value of the line ratio when the galaxy properties vary widely. Indeed, the molecular gas mass calculated for NGC 3034 (M82) is certainly an overestimate because the CO line ratios in this starburst galaxy are much larger (Ward et al. 2003). Similarly, at least two of the bright spirals in Virgo (NGC 4321 and NGC 4254) also show elevated line ratios (Wilson et al. 2009). In contrast, for low-luminosity galaxies the molecular gas mass may be underestimated if the CO excitation is very low. NGC 2841 has been detected in the CO $J = 2{-}1$ line by Leroy et al. (2009); adopting a CO $J = 2{-}1/1{-}0$ line ratio of 0.52 leads to a molecular mass fraction of 0.20, a factor of 10 above the upper limit deduced from the CO $J = 3{-}2$ upper limit. The fact that we have measured upper limits to the CO luminosity over a 1-arcmin diameter aperture, which is roughly a factor of 7 smaller than the area of the galaxy within $D_{25}/2$, may go some way to explaining this discrepancy.

4.2 The $L_{\rm CO(3-2)}$–$L_{\rm FIR}$ correlation

We have used the NGLS CO measurements to examine the correlation between the far-infrared luminosity and the CO $J = 3{-}2$ luminosity. Iono et al. (2009) presented a nearly linear correlation between these two luminosities, and suggested that the CO $J = 3{-}2$ line could be a good tracer of the dense gas involved in star formation, similar to the HCN $J = 1{-}0$ line (Gao & Solomon 2004). We have collected far-infrared luminosities derived from *IRAS* data for all the SINGS galaxies for which such measurements are available. The preferred source is the Revised Bright Galaxy Survey (Sanders et al. 2003) followed by Lisenfeld et al. (2007). For eight additional galaxies we retrieved the 60- and 100-μm fluxes from the *IRAS* Faint Source Catalogue and calculated the far-infrared luminosity using the formula in Lisenfeld et al. (2007). When necessary, published far-infrared luminosities were adjusted for our adopted distances.

Fig. 4 plots the far-infrared luminosity as a function of the CO $J = 3{-}2$ luminosity, while Fig. 5 plots the ratio $L_{\rm FIR}/L_{\rm CO(3-2)}$ as a function of the CO luminosity. These figures reveal a remarkably tight correlation for the more luminous galaxies and increased scatter among the fainter galaxies. Of 19 galaxies with $9.5 < \log L_{\rm FIR} < 10.7$, only NGC 337 is not detected in the CO $J = 3{-}2$ line. In comparison to NGC 2841, which has a lower limit similar to $L_{\rm FIR}/L_{\rm CO(3-2)}$ and which has been detected in the CO 2–1 line (Leroy et al. 2009), NGC 337 is five times more luminous in the infrared yet with a somewhat smaller atomic gas mass and linear extent (as measured by the D_{25} diameter). Despite its inclusion in the SINGS sample (Kennicutt et al. 2003), this galaxy has not been very well studied. One explanation of its unusually high infrared luminosity would be the presence of an active galactic nucleus. However, the *GALEX* images (Gil de Paz et al. 2011) show no hint of a bright nuclear source while the mid-infrared emission is extended and asymmetric (Bendo et al. 2007). Its optical through infrared SED is consistent with a normal spiral galaxy (Dale et al. 2007), optical spectroscopy is dominated by star formation indicators, and the metallicity is near solar (Moustakas et al. 2010). This galaxy remains a bit of a mystery and would be worthy of further study.

Excluding NGC 337, the mean $L_{\rm FIR}/L_{\rm CO(3-2)}$ ratio for the luminous galaxies is 62 ± 5, with a standard deviation of 20. The situation is more complicated for the fainter galaxies. Of 12 galaxies with $8.3 < \log L_{\rm FIR} < 9.5$, only seven (58 per cent) have global CO luminosities that are detected at better than the 4σ level. For these seven galaxies, the mean $L_{\rm FIR}/L_{\rm CO(3-2)}$ is 147 ± 20, with a standard deviation of 53. Some of the increased scatter is likely due to the larger CO measurement uncertainties on these fainter galaxies, but this seems unlikely to explain all the scatter and the increased mean ratio. One possibility is that these lower luminosity and hence likely lower mass galaxies may tend to have lower metallicities, in which case the CO luminosity may systematically underestimate the molecular hydrogen gas mass and cause them to appear underluminous in CO (Israel 1997; Leroy et al. 2011). However, the characteristic oxygen abundance for these lower luminosity galaxies is not significantly different from that of the higher luminosity systems (Moustakas et al. 2010). Another possibility is that these fainter galaxies have lower average CO surface brightnesses, in which case we could be systematically underestimating the CO luminosity due to the low signal-to-noise ratio in the data. An example of this type of effect is seen for NGC 2403, for which

Table 3. CO and far-infrared luminosities for the SINGS sample.

Name	D [a] (Mpc)	ΔT [b] (mK)	$L_{CO(3-2)}$ [c] ($\times 10^7$ K km s^{-1} pc^2)	log L_{FIR} [d] ($L_\odot$)	$L_{FIR}/L_{CO(3-2)}$ $L_\odot$/(K km s^{-1} pc^2)	M_{H_2}/M_{HI} [e]
NGC 0024	7.6	27	<0.4	8.19	>40	<0.10
NGC 0628	7.3	24	5.2 ± 1.0	9.55	67	0.25
NGC 0925	9.1	25	0.9 ± 0.2	9.31	221	0.04
NGC 2403	3.2	23	1.7 ± 0.3	9.09	72	0.12
UGC 04305	3.4	31	<0.09	7.51	>38	<0.02
NGC 2841	14.1	24	<1.1	9.45	>249	<0.02
NGC 2976	3.6	26	0.50 ± 0.08	8.72	103	0.65
NGC 3031	3.6	26	0.91 ± 0.35	9.41	284	0.05
NGC 3034	3.6	31	39.2 ± 0.4	10.60	102	8.6
NGC 3184	11.1	28	9.5 ± 1.4	9.61	43	0.55
NGC 3198	13.7	31	6.9 ± 1.1	9.61	60	0.12
IC 2574	3.8	23	<0.08	–	–	<0.01
NGC 3351	9.3	23	5.1 ± 0.6	9.66	88	0.89
NGC 3521	7.9	27	17.9 ± 1.2	9.97	52	0.73
NGC 3627	9.4	23	31.1 ± 1.7	10.18	49	6.5
NGC 3938	14.7	26	12.3 ± 2.0	9.85	57	0.51
NGC 4236	4.4	21	0.53 ± 0.15	8.19	29	0.05
NGC 4254	16.7	27	73.8 ± 4.8	10.50	43	2.7
NGC 4321	16.7	28	54.7 ± 5.3	10.36	42	3.1
NGC 4450	16.7	23	1.1 ± 0.3	9.06	106	0.62
NGC 4559	9.3	23	1.9 ± 0.4	9.42	138	0.07
NGC 4569	16.7	26	20.1 ± 1.7	9.95	44	5.3
NGC 4579	16.7	20	7.9 ± 1.4	9.84	87	2.3
NGC 4594	9.8	28	<0.7	8.92	>122	<0.43
NGC 4631	7.7	20	14.6 ± 0.7	10.10	85	0.31
NGC 4725	11.9	25	<0.9	–	–	<0.05
NGC 4736	5.2	30	5.2 ± 0.4	9.65	86	1.9
NGC 4826	7.5	30	9.7 ± 0.5	9.75	58	3.3
NGC 5033	16.2	24	23.1 ± 3.0	10.19	67	1.6
NGC 5055	7.9	30	19.7 ± 1.7	10.00	51	0.63
NGC 5194	7.7	15	53.2 ± 2.0	10.21	31	4.0
NGC 0337	23.1	37	<5.6	10.13	>240	<0.15
NGC 0584	20.1	19	<2.5	–	–	<2.6
NGC 0855	9.7	15	<0.5	8.29	>41	<0.54
PGC 023521	3.6	29	<0.1	–	–	<1.4
UGC 05139	3.6	22	<0.09	–	–	<0.12
NGC 3049	22.7	20	1.4 ± 0.3	9.39	176	0.15
UGC 05336	3.6	21	<0.09	–	–	<0.0.05
UGC 05423	3.6	24	<0.1	–	–	<1.5
NGC 3190	21.3	19	<2.7	9.52	>121	<0.86
NGC 3265	22.7	20	<3.3	–	–	<2.7
UGC 05720	25.0	21	2.8 ± 0.6	–	–	0.70
NGC 3773	10.5	16	0.20 ± 0.05	8.38	122	0.54
NGC 4625	9.4	19	0.12 ± 0.03	8.37	196	0.03
NGC 4789A	3.8	7.3	<0.03	–	–	<0.02
UGC 08201	4.6	18	<0.1	–	–	<0.19
NGC 5474	6.5	26	<0.3	8.14	>40	<0.06

[a]NGC 925, NGC 2403, NGC 3031, NGC 3198, NGC 3351, NGC 3627, NGC 4725: Freedman et al. (2001); NGC 2976, NGC 4236, UGC 04305, UGC 08201: Karachentsev et al. (2002); NGC 3034, PGC 023521, UGC 05139, UGC 05336, UGC 05423: same distance as NGC 3031 (Freedman et al. 2001); NGC 584, NGC 855, NGC 4594, NGC 4736, NGC 4826, NGC 5194: Tonry et al. (2001); Virgo cluster: Mei et al. (2007); NGC 628: Karachentsev et al. (2004); IC 2574: Dalcanton et al. (2009); NGC 2841: Macri et al. (2001); NGC 3184: Leonard et al. (2002); NGC 4631: Seth, Dalcanton & de Jong (2005). Remaining galaxies: Hubble flow distance with velocity corrected for Virgo infall (Mould et al. 2000) and $H_0 = 70.5$ km s^{-1} Mpc^{-1}.
[b]rms noise in individual spectra in the data cube at 20 km s^{-1} resolution on T_{MB} scale.
[c]Upper limits are 2σ limits calculated over an area of 1 arcmin and a line width of 100 km s^{-1}.
[d] L_{FIR} from Sanders et al. (2003) and Lisenfeld et al. (2007) (see text) adjusted for distances given here.
[e]Total H I masses (including emission from areas outside the CO disc) from fluxes in Walter et al. (2008), Chung et al. (2009), or the HyperLeda data base (Paturel et al. 2003); see text. M_{H_2} calculated assuming a CO $J = 3{-}2/J = 1{-}0$ line ratio of 0.18, which may overestimate the total mass in some galaxies, as well as a standard value for X_{CO}; see text.

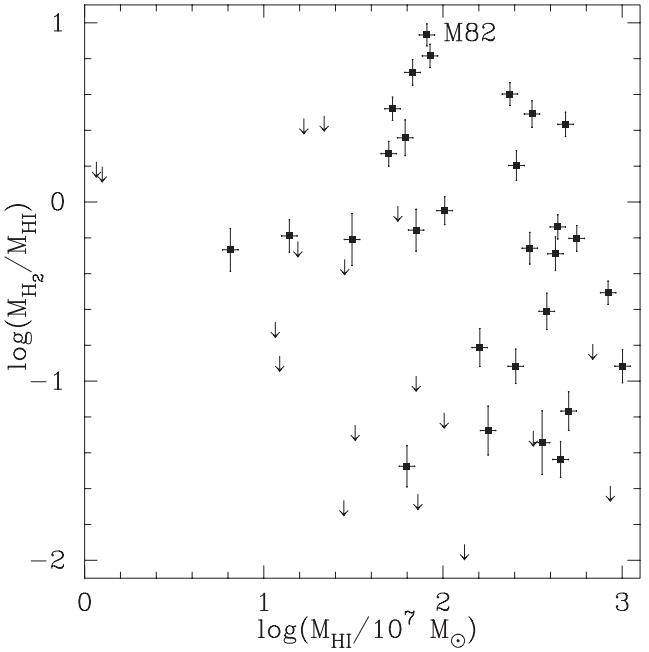

Figure 3. The ratio of H_2 to H I mass plotted as a function of H I mass. Galaxies with only upper limits to the CO luminosity are shown as arrows. H_2 masses have been calculated assuming a CO $J = 3{-}2/J = 1{-}0$ line ratio of 0.18; this line ratio may not be appropriate for all galaxies, particularly the more luminous ones such as NGC 3034 (M82).

the CO luminosity increases by more than a factor of 2 when the moment maps are made with a 2σ cut-off compared to a 3σ cut-off (see Section 2.2). This increase occurs because the CO emission in NGC 2403 is very close to the noise limit over a large area of the galaxy. Finally, if these lower luminosity galaxies tend to have systematically lower star formation rate surface densities, the excitation of the CO 3–2 line relative to the ground state line may be lower than in the more luminous galaxies, which would again cause them to appear underluminous in CO $J = 3{-}2$ (but perhaps not in CO $J = 1{-}0$).

We can use the average $L_{\rm FIR}/L_{\rm CO(3-2)}$ ratio to make a crude estimate of the global molecular gas depletion time in the spiral galaxies in our sample. We can convert $L_{\rm CO(3-2)}$ to molecular gas mass $M_{\rm mol} = 1.36 M_{\rm H_2}$ using equation (5) and $L_{\rm FIR}$ to star formation rate (SFR) using equation (4) from Kennicutt (1998). We note that this star formation rate equation is only strictly appropriate for starburst galaxies, in particular because the far-infrared luminosity may include a contribution from dust heated by older stars; see Kennicutt (1998) for further details. We further convert from $L_{\rm IR}$ used in Kennicutt (1998) to $L_{\rm FIR}$ by adopting $L_{\rm IR} = 1.3 L_{\rm FIR}$ (Graciá-Carpio et al. 2008) and convert to the double-power-law initial mass function used by Calzetti et al. (2007) to give $\mathrm{SFR} = 1.3 \times 10^{-10} L_{\rm FIR}$ with SFR in $\mathrm{M_\odot\ yr^{-1}}$ and $L_{\rm FIR}$ in $\mathrm{L_\odot}$. With these two equations, the average $L_{\rm FIR}/L_{\rm CO(3-2)}$ ratio of 62 ± 5 corresponds to a molecular gas depletion time of 3.0 ± 0.3 Gyr. Despite the uncertainties inherent in this calculation, this mean value is in line with the recent estimate of the molecular gas depletion time of 2.35 Gyr by Bigiel et al. (2011). The agreement is even more striking when we consider that the two analyses use different CO data, different data to trace the star formation rate, and one is a global measurement while the other is based on resolved measurements.

In contrast to this star formation rate analysis, Bendo et al. (2010b, 2012) and others have presented evidence that much of the dust emission is at least partially heated by a more quiescent stellar population. Even at wavelengths as short as 60 and 100 μm, there can be a significant contribution to dust heating from the general interstellar radiation field; one of the most spectacular examples of

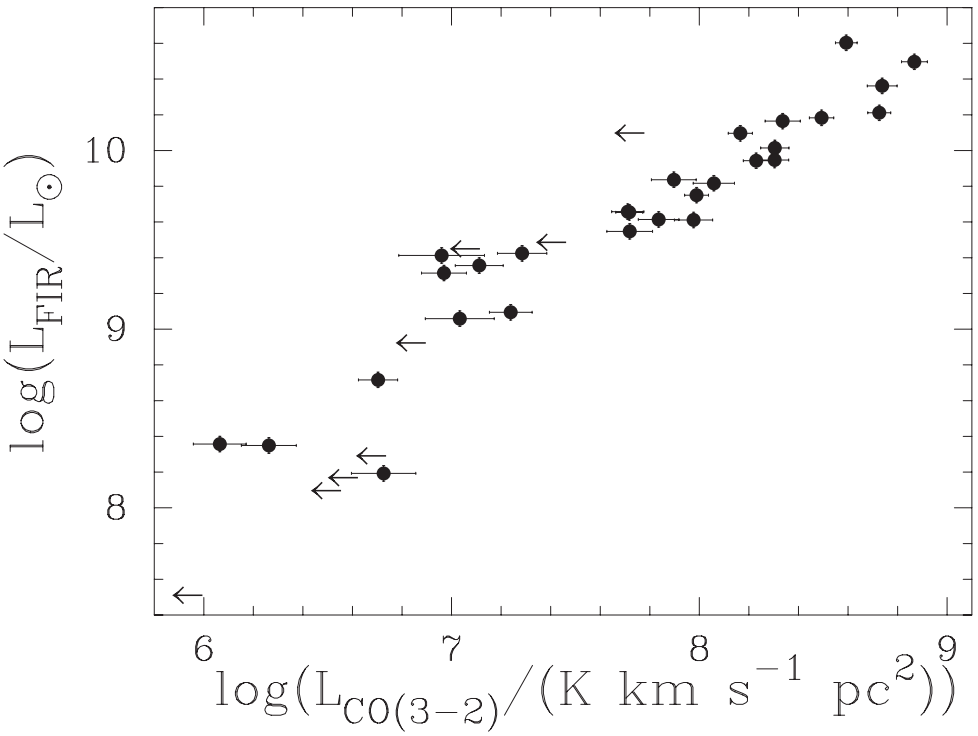

Figure 4. $L_{\rm FIR}$ plotted versus $L_{\rm CO(3-2)}$ for all SINGS galaxies in the NGLS with far-infrared data. Galaxies which were not detected in CO are indicated by arrows.

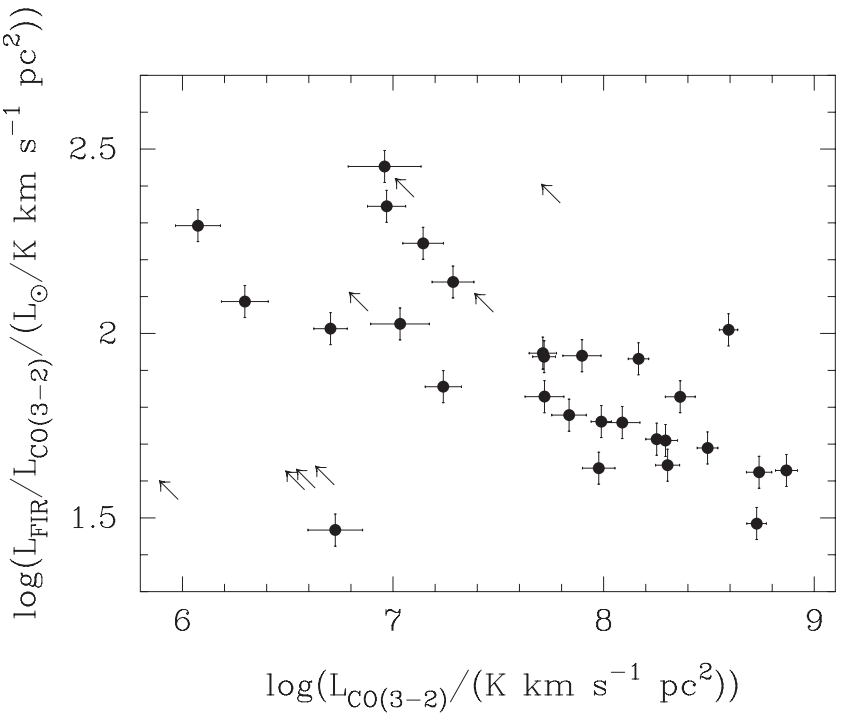

Figure 5. $L_{FIR}/L_{CO(3-2)}$ plotted versus $L_{CO(3-2)}$ for all SINGS galaxies in the NGLS with far-infrared data. Galaxies which were not detected in CO are indicated by arrows.

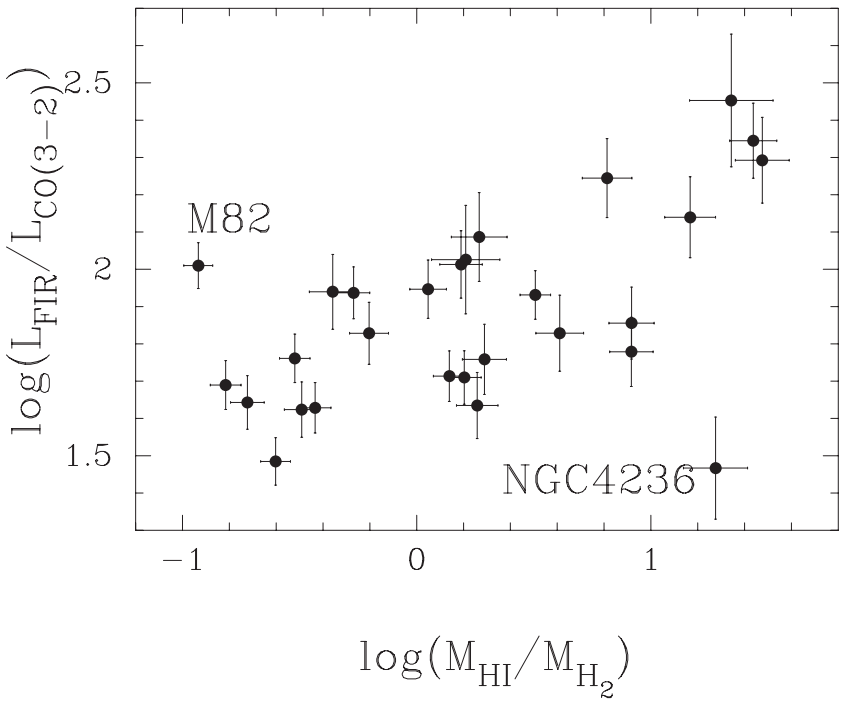

Figure 6. $L_{FIR}/L_{CO(3-2)}$ plotted versus M_{HI}/M_{H_2} for all SINGS galaxies in the NGLS with far-infrared data. Galaxies which were not detected in CO are omitted from this figure.

this phenomenon is M31, in which 90 per cent of the dust emission is not directly associated with star formation (Walterbos & Schwering 1987). Since the far-infrared luminosity is also related to the total mass of dust, a plot of L_{FIR} versus L_{CO} may be primarily probing the molecular gas-to-dust mass ratio in galaxies. Fig. 6 shows the $L_{FIR}/L_{CO(3-2)}$ ratio plotted as a function of relative mass fractions of atomic and molecular gas, M_{H1}/M_{H_2}. The two ratios are correlated at better than the 99 per cent level, even when outliers such as M82 and NGC 4236 are included. If the far-infrared emission originated purely in dust associated with the molecular phase of the ISM traced by the CO $J = 3-2$ line, we would expect no correlation in this plot. At the opposite extreme, if the far-infrared emission

originated purely in dust associated with the atomic phase of the ISM, we would expect a slope of unity. The observed slope of ∼0.2–0.3 suggests that some of the far-infrared emission is originating in dust associated with atomic gas or perhaps with more diffuse molecular gas that does not emit strongly in the CO $J = 3{-}2$ line, and that this is a particularly important effect in galaxies where the ISM is predominantly atomic. Galaxies in the upper right portion of the figure tend to be either very early or very late-type spiral galaxies. We note that if the H_2 mass is underestimated in some of these galaxies due to low metallicity, this effect would tend to steepen the slope and not remove the observed trend. One additional complication in interpreting this figure is that the spatial extent of the atomic gas tends to be much larger than the CO or the far-infrared emission. The atomic gas is distributed in a roughly constant surface density disc, while the dust and molecular gas trace more of an exponential disc.

4.3 $L_{CO(3-2)}$ and L_{FIR} at low and high redshift

Iono et al. (2009) presented a detailed comparison of the CO $J = 3{-}2$ luminosity for a sample of local ($D < 200$ Mpc) luminous and ultraluminous infrared galaxies with a high-redshift sample of submillimetre galaxies, quasars and Lyman-break galaxies. Including a small sample of local star-forming galaxies, they found a strong and nearly linear correlation of $L_{CO(3-2)}$ and L_{FIR} over nearly five orders of magnitude, which suggested the star formation efficiency was constant to within a factor of 2 across many different types of galaxies and epochs. One limitation of the analysis was that the sample of local galaxies used was relatively small (14) and the data were limited to a single central pointing (Mauersberger 1999; Komugi et al. 2007). In addition, the far-infrared luminosity for the 22-arcsec diameter aperture was calculated from an Hα-derived star formation rate. With the larger sample available here, we are in a good position to re-examine this relation, and to do so using global galaxy luminosities across all redshifts and luminosities.

Fig. 7 plots L_{FIR} versus $L_{CO(3-2)}$ and also the ratio $L_{FIR}/L_{CO(3-2)}$ for both the NGLS with the (Ultra) Luminous Infrared Galaxies (U/LIRG) and high-redshift galaxy sample from Iono et al. (2009). This plot shows a significant trend of the $L_{FIR}/L_{CO(3-2)}$ ratio as a function of the CO luminosity. The mean $L_{FIR}/L_{CO(3-2)}$ for galaxies with $\log L_{FIR} > 11$ from the local U/LIRG and high-redshift samples is 320 ± 40 with a standard deviation of 240. This is a factor of 5 larger than the mean ratio of 60 measured for NGLS galaxies with $9.5 < \log L_{FIR} < 10.7$. We can again convert $L_{FIR}/L_{CO(3-2)}$ to a molecular gas depletion time, but this time using the CO-to-H_2 conversion factor (0.8) and CO $J = 3{-}2/J = 1{-}0$ line ratio (0.5) appropriate for ULIRGs (Wilson et al. 2008). Using equation (3) from Wilson et al. (2008) and the same star formation rate equation from Kennicutt (1998) modified as described above, the $L_{FIR}/L_{CO(3-2)}$ ratio of 320 corresponds to a molecular gas depletion time of only 50 Myr, more than a factor of 50 smaller than the ratio for normal disc galaxies. A fit to the data for galaxies with $L_{CO(3-2)} > 7.5$ (or $\log L_{FIR} > 9.5$) gives a slope of ∼0.2, which is consistent with a ∼3 times higher line ratio for 10^{12} $L_\odot$ and a ∼5 times higher line ratio for 10^{13} $L_\odot$ than for a typical local disc galaxy with $L_{FIR} = 10^{10}$ $L_\odot$.

Recently, Genzel et al. (2010) have analysed the star formation properties of a sample of low- and high-redshift galaxies, with one part of their analysis examining the $L_{FIR}/L_{CO(1-0)}$ ratio. Their study combined CO $J = 1{-}0$ data for redshift zero galaxies with CO $J = 1{-}0$ values for high-redshift galaxies that have been inferred from observations of the CO $J = 2{-}1$, $J = 3{-}2$ and $J = 4{-}3$ transitions assuming appropriate line ratios for each type of galaxy. They also used a variety of star formation rate tracers, which were then converted to L_{FIR} using the same equations as we have adopted above. A similar analysis with a somewhat different high-redshift sample has also been published by Daddi et al. (2010). Given the various assumptions and conversions in these analyses of the $L_{FIR}/L_{CO(1-0)}$ ratio, it is useful to compare their results with our results which are based on direct measurements of both the CO and the far-infrared luminosities without any need for additional corrections.

The difference in the $L_{FIR}/L_{CO(3-2)}$ ratio of a factor of 5 between normal low-redshift galaxies and mergers at both low and high redshift is consistent with the mean difference of 5.4 between the average $L_{FIR}/L_{CO(1-0)}$ ratio of normal galaxies and merging galaxies seen by Genzel et al. (2010). The normal galaxy average value includes galaxies at both low and high redshifts. When these data are converted to a gas depletion time, the average for the low-redshift galaxies is 1.5 Gyr while the average for the high-redshift galaxies is 0.5 Gyr. Using the average $L_{FIR}/L_{CO(1-0)}$ ratio given in fig. 2 of Genzel et al. (2010), we calculate an overall average depletion time of 1.2 Gyr for the normal galaxies across all redshifts, which suggests that the $L_{FIR}/L_{CO(1-0)}$ ratio of the low- and high-redshift mergers is ∼7 times higher than that of normal galaxies at $z = 0$ alone. Interestingly, the average $L_{FIR}/L_{CO(1-0)}$ ratio given in fig. 2 of Genzel et al. (2010) for the mergers implies a gas depletion time of only 70 Myr,[5] quite consistent with our estimate of 50 Myr from the $L_{FIR}/L_{CO(3-2)}$ ratio. Overall, the analysis presented here is complementary to that of Genzel et al. (2010) and provides some evidence that the conversions between CO transitions and different star formation rate tracers used in Genzel et al. (2010) have not biased the high-redshift analysis.

5 CONCLUSIONS

The James Clerk Maxwell Telescope NGLS comprises an H I-selected sample of 155 galaxies spanning all morphological types with distances less than 25 Mpc. We have used new, large-area CO $J = 3{-}2$ maps from the NGLS to examine the molecular gas mass fraction and the correlation between far-infrared and CO luminosity using 47 galaxies drawn from the SINGS sample (Kennicutt et al. 2003). We find a good correlation of the CO $J = 3{-}2$ luminosity with the CO $J = 2{-}1$ luminosity (Leroy et al. 2009) and the CO $J = 1{-}0$ luminosity (Kuno et al. 2007), with average global line ratios of 0.18 ± 0.02 for the CO $J = 3{-}2/J = 1{-}0$ line ratio and 0.36 ± 0.04 for the CO $J = 3{-}2/2{-}1$ line ratio. The galaxies in our sample span a wide range of ISM mass and molecular gas mass fraction, with 21 per cent of the galaxies in the sample having more molecular than atomic gas and 60 per cent having molecular to atomic mass ratios less than 0.5.

We explore the correlation of the far-infrared luminosity, which traces star formation, with the CO luminosity, which traces the molecular gas mass. We find that the more luminous galaxies in our sample (with $\log L_{FIR} > 9.5$ or $\log L_{CO(3-2)} > 7.5$) have a uniform $L_{FIR}/L_{CO(3-2)}$ ratio of 62 ± 5. The lower luminosity galaxies show a wider range of the $L_{FIR}/L_{CO(3-2)}$ ratio and many of these galaxies are not detected in the CO $J = 3{-}2$ line. We can convert this

[5] Note that while (Genzel et al. 2010) give a gas depletion time of 200 Myr for these data, it appears that their calculation of this particular number neglected to take into account the smaller CO-to-H_2 conversion factor appropriate for merger galaxies.

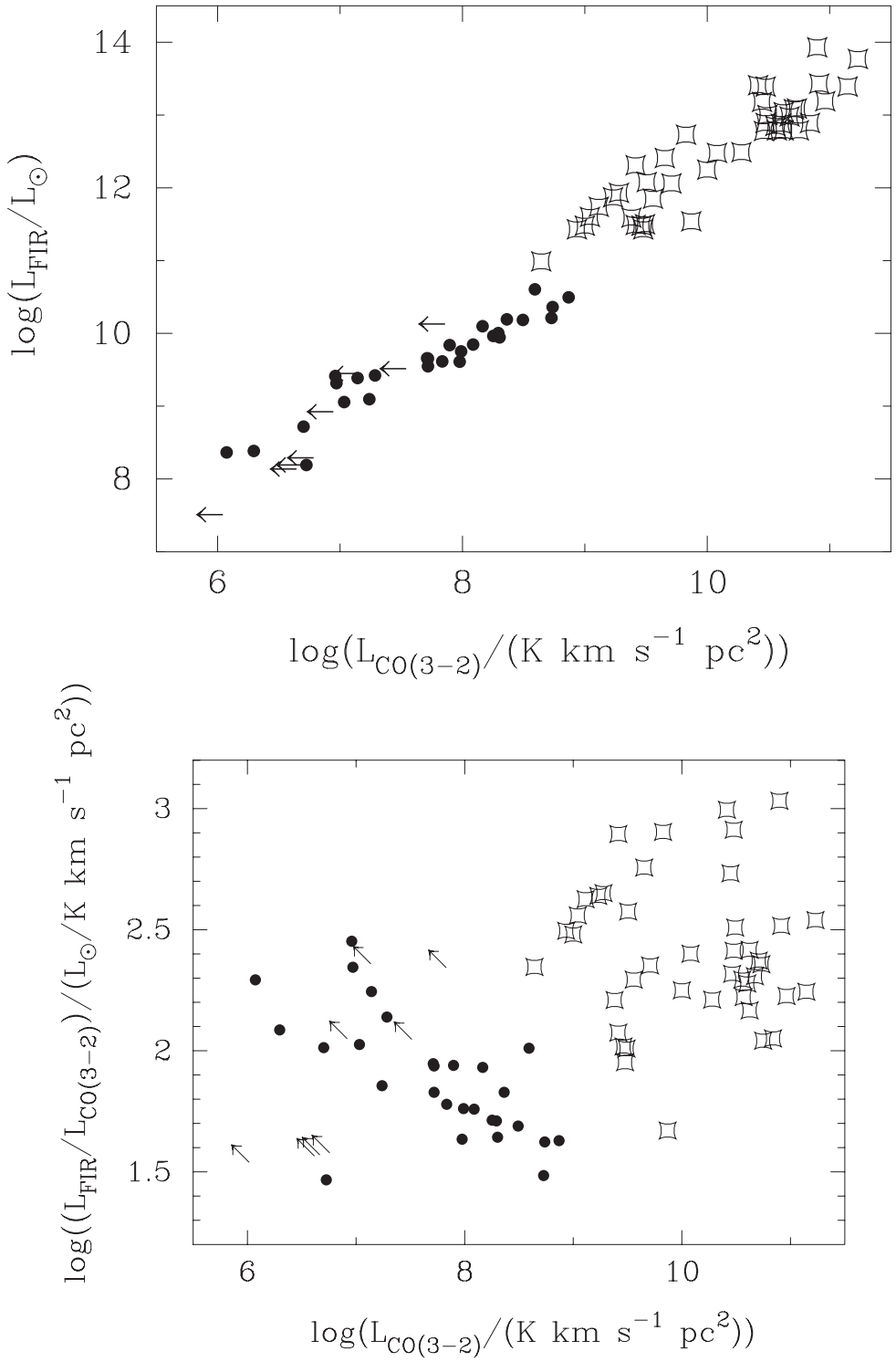

Figure 7. Top: $\log L_{FIR}$ plotted versus $\log L_{CO(3-2)}$ for all SINGS galaxies in the NGLS with far-infrared data (filled symbols and arrows; see Fig. 5). The local U/LIRG and high-redshift samples from Iono et al. (2009) are plotted as the open symbols. Bottom: $\log L_{FIR}/L_{CO(3-2)}$ plotted versus $\log L_{CO(3-2)}$ for the same set of galaxies.

luminosity ratio to a molecular gas depletion time and find a value of 3.0 ± 0.3 Gyr, in good agreement with recent estimates from Bigiel et al. (2011). We also find a correlation of the $L_{FIR}/L_{CO(3-2)}$ ratio with the mass ratio of atomic to molecular gas, which suggests that some of the far-infrared emission originates from dust associated with the atomic gas. This effect is particularly important in galaxies where the gas is predominantly atomic.

By comparing the NGLS data with merging galaxies at low and high redshift from the sample of Iono et al. (2009), which have also been observed in the CO $J = 3-2$ line, we show that the

$L_{FIR}/L_{CO(3-2)}$ ratio shows a significant trend with luminosity and thus that the correlation of L_{FIR} with $L_{CO(3-2)}$ is not as linear a trend as found by Iono et al. (2009). Taking into account differences in the CO $J = 3-2/J = 1-0$ line ratio and the CO-to-H_2 conversion factor between the mergers and the normal disc galaxies, this trend in the $L_{FIR}/L_{CO(3-2)}$ ratio is consistent with a molecular gas depletion time of only 50 Myr in the merger sample, roughly 60 times shorter than in the nearby normal galaxies.

ACKNOWLEDGMENTS

The James Clerk Maxwell Telescope is operated by The Joint Astronomy Centre on behalf of the Science and Technology Facilities Council of the United Kingdom, the Netherlands Organisation for Scientific Research and the National Research Council of Canada. The research of PB, PC, S. Courteau, MF, MH, JI,ER, ES, KS, TW and CDW is supported by grants from NSERC (Canada). AU has been supported through a Post Doctoral Research Assistantship from the UK Science and Technology Facilities Council. Travel support for BEW and TW was supplied by the National Research Council (Canada). We acknowledge the usage of the HyperLeda data base (http://leda.univ-lyon1.fr). CV received support from the ALMA-CONICYT Fund for the Development of Chilean Astronomy (Project 31090013) and from the Center of Excellence in Astrophysics and Associated Technologies (PBF 06). This research has made use of the NASA/IPAC Extragalactic Database (NED) which is operated by the Jet Propulsion Laboratory, California Institute of Technology, under contract with the National Aeronautics and Space Administration.

REFERENCES

Ade P. A. R. et al., 2011, A&A, 536, 17
Alton P. B., Bianchi S., Richer J., Pierce-Price D., Combes F., 2002, A&A, 388, 446
Arimoto N., Sofuie Y., Tsujimot T., 1996, PASJ, 48, 275
Arzoumanian D. et al., 2011, A&A, 529, L6
Bendo G. J. et al., 2006, ApJ, 652, 283
Bendo G. J. et al., 2007, MNRAS, 380, 1313
Bendo G. J. et al., 2010a, MNRAS, 402, 1409
Bendo G. J. et al., 2010b, A&A, 518, L65
Bendo G. J. et al., 2012, MNRAS, 419, 1833
Berry D. S., Reinhold K., Jenness T., Economou F., 2007, in Shaw R. A., Hill F., Bell D. J., eds, ASP Conf. Ser. Vol. 376, Astronomical Data Analysis Software and Systems XVI. Astron. Soc. Pac., San Francisco, p. 425
Bigiel F. et al., 2008, AJ, 136, 2846
Bigiel F. et al., 2011, ApJ, 730, L13
Bolatto A., Leroy A. K., Rosolowsky E., Walter F., Blitz L., 2008, ApJ, 686, 948
Boselli A. et al., 2010, PASP, 122, 261
Bot C. et al., 2010, A&A, 523, A20
Braine J., Combes F., Casoli F., Dupraz C., Gerin M., Klein U., Wielebinski R., Brouillet N., 1993, A&AS, 97, 887
Braine J. et al., 1997, A&A, 326, 963
Bregman J. N., Snider B. A., Grego L., Cox C. V., 1998, ApJ, 499, 670
Buckle J. V. et al., 2009, MNRAS, 399, 1026
Buta R. J., Corwin H. G., Odewahn S. C., 2007, The de Vaucouleurs Atlas of Galaxies. Cambridge Univ. Press, Cambridge
Calzetti D. et al., 2007, ApJ, 666, 870
Cannon J. M. et al., 2011, ApJ, 735, 36
Chung A., van Gorkom J. H., Kenney J. D. P., Crowl H., Vollmer B., 2009, AJ, 138, 1741
Combes F., Becquaert J.-F., 1997, A&A, 327, 453
Currie M. J., Draper P. W., Berry D. S., Jenness T., Cavanagh B., Economou F., 2008, in Argyle R. W., Bunclark P. S., Lewis J. R., eds, ASP Conf. Ser. Vol. 394, Astronomical Data Analysis Software and Systems. Astron. Soc. Pac., San Francisco, p. 650
Daddi E. et al., 2010, ApJ, 714, L118
Dalcanton J. J. et al., 2009, ApJS, 183, 67
Dale D. A. et al., 2007, ApJ, 655, 863
Davies J. et al., 2004, MNRAS, 349, 922
Davies J. I. et al., 2010, A&A, 518, L48
de Vaucoulers G., de Vaucoulers A., Corwin H. G., Buta R. J., Paturel G., Fouqué P., 1991, Third Reference Catalogue of Bright Galaxies. Springer, New York
Downes D., Solomon P. M., 1998, ApJ, 507, 615
Dumke M., Nieten C., Thuma G., Wielebinski R., Walsh W., 2001, A&A, 373, 853
Dunne L., Eales S., Edmunds M., Ivison R., Alexander P., Clements D. L., 2000, MNRAS, 315, 115
Eales S. et al., 2010, A&A, 518, L62
Elmegreen B. G., Elmegreen D. M., 1986, ApJ, 311, 554
Foyle K., Rix H.-W., Walter F., Leroy A. K., 2010, ApJ, 725, 534
Freedman W. L. et al., 2001, ApJ, 553, 47
Galliano F., Madden S. C., Jones A. P., Wilson C. D., Bernard J.-P., Le Peintre F., 2003, A&A, 407, 159
Galliano F., Madden S. C., Jones A. P., Wilson C. D., Bernard J.-P., 2005, A&A, 434, 867
Galliano F. et al., 2011, A&A, 536, A88
Gao Y., Solomon P. M., 2004, ApJ, 606, 271
Genzel R. et al., 2010, MNRAS, 407, 2091
Gil de Paz A. et al., 2011, ApJS, 173, 185
Giovanelli R. et al., 2005, AJ, 130, 2613
Graciá-Carpio J., García-Burillo S., Planesas P., Fuente A., Usero A., 2008, A&A, 479, 703
Helfer T. T., Blitz L., 1993, ApJ, 419, 86
Helfer T. T., Thornely M. D., Regan M. W., Wong T., Sheth K., Vogel S. N., Blitz L., Bock D. C.-J., 2003, ApJS, 145, 259
Iono D. et al., 2009, ApJ, 695, 1537
Irwin J. et al., 2011, MNRAS, 419, 1423
Israel F. P., 1997, A&A, 328, 471
Johnstone D., Wilson C. D., Moriarty-Schieven G., Joncas G., Smith G., Gregersen E., Fich M., 2000, ApJ, 545, 327
Karachentsev I. D. et al., 2002, A&A, 383, 125
Karachentsev I. D., Karachentseva V. E., Huchtmeier W. K., Makarove D. I., 2004, AJ, 127, 2031
Kennicutt R. C., 1989, ApJ, 344, 685
Kennicutt R. C., 1998, ARA&A, 36, 189
Kennicutt R. C. et al., 2003, PASP, 115, 928
Kennicutt R. C. et al., 2007, ApJ, 671, 333
Kennicutt R. C. et al., 2011, PASP, 123, 1347
Knapp G. R., Guhathakurta P., Kim D.-W., Jura M. A., 1989, ApJS, 70, 329
Komugi S., Kohno K., Tosaki T., Nakanishi H., Onodera S., Egusa F., Sofue Y., 2007, PASJ, 59, 55
Kuno N. et al., 2007, PASJ, 59, 117
Lada E. A., Bally J., Stark A. A., 1991a, ApJ, 368, 432
Lada E. A., Depoy D. L., Evans N. J., Gatley I., 1991b, ApJ, 371, 171
Lee S.-W., Irwin J. A., 1997, ApJ, 490, 247
Lee H., McCall M. L., Richer M. G., 2003, AJ, 125, 2975
Leech J., Isaak K. G., Papadopoulos P. P., Gao Y., Davis G. R., 2010, MNRAS, 406, 1364
Leonard D. C. et al., 2002, AJ, 124, 2490
Leroy A. K., Walter F., Brinks E., Bigiel F., de Blok W. J. G., Madore B., Thornley M. D., 2009, AJ, 136, 2782
Leroy A. K. et al., 2009, AJ, 137, 4670
Leroy A. K. et al., 2011, ApJ, 737, 12
Lisenfeld U. et al., 2002, A&A, 382, 860
Lisenfeld U. et al., 2007, A&A, 462, 507
Macri L. M., Stetson P. B., Bothun G. D., Freedman W. L., Garnavich P. M., Jha S., Madore B. F., Richmond M. W., 2001, ApJ, 559, 243

Madden S. C., Poglitsch A., Geis N., Stacey G. J., Townes C. H., 1997, ApJ, 483, 200
Madden S. C., Galliano F., Jones A. P., Sauvage M., 2006, A&A, 446, 877
Mao R. Q., Schulz A., Henkel C., Mauersberger R., Muders D., Trung D. V., 2010, ApJ, 724, 1336
Martin M. C., 1998, A&AS, 131, 77
Mauersberger R., Henkel C., Walshi W., Schulz A., 1999, A&A, 341, 256
Mei S. et al., 2007, ApJ, 655, 144
Meier D. S., Turner J. L., Crosthwaite L. P., Beck S. C., 2001, AJ, 121, 740
Moore B., Lake G., Katz N., 1998, ApJ, 495, 139
Mould J. R. et al., 2000, ApJ, 529, 786
Moustakas J., Kennicutt R. C., Tremonti C. A., Dale D. A., Smith J.-D. T., Calzetti D., 2010, ApJS, 190, 233
Muñoz-Mateos J. C. et al., 2009, ApJ, 703, 1569
Muraoka K. et al., 2007, PASJ, 59, 43
O'Halloran B. et al., 2010, A&A, 518, L58
Papadopoulos P. P., van der Werf P., Xilouris E. M., Isaak K. G., Gao Y., Muehle S., 2012, ApJ, 751, 10
Paturel G., Theureau G., Bottinelli L., Gouguenheim L., Coudreau-Durand N., Hallet N., Petit C., 2003, A&A, 412, 57
Rosolowsky E., Keto E., Matsushita S., Willner S. P., 2007, ApJ, 661, 830
Roussel H. et al., 2010, A&A, 518, L66
Sanchez-Gallego J. R. et al., 2011, A&A, 527, 16
Sanders D. B., Mirabel F., 1996, ARA&A, 34, 749
Sanders D. B., Mazzarella J. M., Kim D.-C., Surace J. A., Soifer B. T., 2003, AJ, 126, 1607
Seth A. C., Dalcanton J. J., de Jong R. S., 2005, AJ, 129, 1331
Strong A. W. et al., 1988, A&A, 207, 1
Tacconi L. J. et al., 2008, ApJ, 680, 246
Tacconi L. J. et al., 2010, Nat, 463, 781
Thronson H. A., 1988, in Pudritz R. E., Fich M., eds, Galactic and Extragalactic Star Formation. NATO ASI 232. Kluwer, Dordrecht, p. 621
Tonry J. L., Dressler A., Blakeslee J. P., Ajhar E. A., Fletcher A. B., Luppino G. A., Metzger M. R., Moore C. B., 2001, ApJ, 546, 681
Tosaki T., Miura R., Sawada T., Kuno N., Nakanishi K., Kohno K., Okumura S. K., Kawabe R., 2007, ApJ, 664, L27
Vlahakis C., Dunne L., Eales S., 2005, MNRAS, 364, 1253
Vogel S. N., Kulkarni S. R., Scoville N. Z., 1988, Nature, 334, 402
Walter F., Brinks E., de Blok W. J. G., Bigiel F., Kennicutt R. C., Thornley M. D., Leroy A. K., 2008, AJ, 136, 2563
Walterbos R. A. M., Schwering P. B. W., 1987, A&A, 180, 27
Ward J. S., Zmuidzinas J., Harris A. I., Isaak K. G., 2003, ApJ, 587, 171
Warren B. E. et al., 2010, ApJ, 714, 571
Williams J. P., de Geus E. J., Blitz L., 1994, ApJ, 428, 693
Wilson C. D., 1995, ApJ, 448, L97
Wilson C. D., Walker C. E., 1994, ApJ, 432, 148
Wilson C. D., Walker C. E., Thornley M. D., 1997, ApJ, 483, 210
Wilson C. D. et al., 2008, ApJS, 178, 189
Wilson C. D. et al., 2009, ApJ, 693, 1736
Wilson C. D. et al., 2011, MNRAS, 419, 1409
Young J. S. et al., 1995, ApJS, 98, 219
Zavagno A. et al., 2010, A&A, 518, L101
Zhu M. et al., 2009, ApJ, 706, 941

APPENDIX A: FIELD AND VIRGO GALAXY MEMBERSHIP IN THE NGLS

The galaxies chosen to constitute the field and Virgo samples are listed in Tables A1 and A2. Note that not every Virgo galaxy with an H I detection will be included in our sample because of the H I flux limit and the constraints on the size of the sample. See Section 2.1 for more details.

Table A1. Field galaxies in the NGLS.

Name	α(J2000.0)[a] (h:m:s)	δ(J2000.0)[a] (°:′:″)	V_{hel} [b] (km s^{-1})
ESO 538−024	00:10:17.9	−18:15:54	1551
NGC 0210	00:40:35.1	−13:52:26	1663
NGC 0216	00:41:26.8	−21:02:45	1541
IC 0051	00:46:24.3	−13:26:32	1753
NGC 0274	00:51:01.7	−07:03:22	1773
NGC 0404	01:09:27.0	+35:43:04	18
NGC 0450	01:15:30.9	−00:51:38	1829
NGC 0473	01:19:55.1	+16:32:40	2222
NGC 0615	01:35:05.7	−07:20:25	1948
ESO 477−016	01:56:16.0	−22:54:04	1646
NGC 1036	02:40:29.0	+19:17:49	802
NGC 1140	02:54:33.6	−10:01:42	1492
NGC 1156	02:59:42.8	+25:14:27	383
ESO 481−019	03:18:43.3	−23:46:55	1480
NGC 1325	03:24:25.6	−21:32:38	1646
NGC 2146A	06:23:54.3	+78:31:50	1386
NGC 2742	09:07:33.5	+60:28:45	1285
NGC 2787	09:19:19.1	+69:12:12	695
UGC 05272	09:50:22.4	+31:29:16	524
NGC 3077	10:03:20.1	+68:44:01	−14
NGC 3162	10:13:31.6	+22:44:15	1384
NGC 3227	10:23:30.7	+19:51:54	1131
NGC 3254	10:29:20.1	+29:29:32	1262
NGC 3353	10:45:22.4	+55:57:37	941
NGC 3413	10:51:20.7	+32:45:59	667
NGC 3447B	10:53:29.8	+16:47:02	1023
UGC 06029	10:55:02.3	+49:43:33	1403
NGC 3507	11:03:25.4	+18:08:07	967
UGC 06161	11:06:49.9	+43:43:25	804
ESO 570−019	11:20:12.2	−21:28:14	1249
UGC 06378	11:22:08.3	+69:37:54	1309
UGC 06566	11:35:43.6	+58:11:33	1249
NGC 3741	11:36:05.8	+45:17:03	223
UGC 06578	11:36:36.8	+00:49:00	1178
NGC 3782	11:39:20.6	+46:30:51	748
UGC 06792	11:49:23.3	+39:46:15	832
NGC 3931	11:51:13.4	+52:00:03	929
NGC 3928	11:51:47.7	+48:40:59	951
NGC 3998	11:57:56.2	+55:27:13	1099
NGC 4013	11:58:31.5	+43:56:49	744
IC 0750	11:58:52.0	+42:43:19	694
UGC 07009	12:01:44.0	+62:19:40	1097
NGC 4041	12:02:12.2	+62:08:14	1221
NGC 4117	12:07:46.2	+43:07:35	886
NGC 4138	12:09:29.8	+43:41:07	908
NGC 4190	12:13:44.2	+36:37:53	192
IC 3105	12:17:33.7	+12:23:14	−159
NGC 4288	12:20:38.3	+46:17:31	556
UGC 07428	12:22:02.7	+32:05:41	1170
UGC 07512	12:25:41.1	+02:09:35	1505
NGC 4504	12:32:17.5	−07:33:48	1000
NGC 4550	12:35:30.7	+12:13:15	409
UGC 07827	12:39:39.0	+44:49:12	552
PGC 043211	12:47:59.9	+10:58:32	1140
NGC 4772	12:53:29.1	+02:10:05	998
NGC 4941	13:04:13.0	−05:33:06	1108
PGC 045195	13:04:31.2	−03:34:20	1362
UGC 08303	13:13:17.9	+36:12:56	929
ESO 508−030	13:14:55.2	−23:08:44	1510
NGC 5477	14:05:33.2	+54:27:40	328
NGC 5486	14:07:25.1	+55:06:10	1368

Table A1 – *continue*.

Name	α(J2000.0)[a] (h:m:s)	δ(J2000.0)[a] (°:′:″)	$V_{\rm hel}$ [b] (km s^{-1})
PGC 140287	14:16:57.3	+03:50:03	1497
IC 1024	14:31:27.1	+03:00:29	1411
NGC 5701	14:39:11.1	+05:21:49	1524
IC 1066	14:53:02.9	+03:17:45	1581
PGC 057723	16:17:15.8	−11:43:54	934
NGC 6140	16:20:58.0	+65:23:23	866
NGC 6118	16:21:48.6	−02:17:02	1611
PGC 058661	16:38:08.9	−04:49:23	1581
IC 1254	17:11:33.5	+72:24:07	1283
NGC 7465	23:02:01.0	+15:57:53	1972
NGC 7742	23:44:15.8	+10:46:01	1677

[a]From RC3 (de Vaucouleurs et al. 1991).
[b]Systemic velocity from the H I line (heliocentric).

Table A2. Small Virgo galaxies in the NGLS.

Name	α(J2000.0)[a] (h:m:s)	δ(J2000.0)[a] (°:′:″)	$V_{\rm hel}$ [b] (km s^{-1})
PGC 039265	12:16:00.4	04:39:04	2198
NGC 4241	12:18:00.1	06:39:07	733
NGC 4262	12:19:30.6	14:52:39	1363
IC 3155	12:19:45.3	06:00:21	2209
NGC 4268	12:19:47.2	05:17:01	2169
NGC 4270	12:19:49.5	05:27:48	2351
NGC 4277	12:20:03.8	05:20:29	2398
NGC 4298	12:21:32.8	14:36:22	1126
NGC 4301	12:22:27.3	04:33:58	1275
NGC 4318	12:22:43.4	08:11:54	1227
NGC 4324	12:23:05.9	05:14:59	1685
NGC 4376	12:25:18.1	05:44:28	1161
NGC 4383	12:25:25.6	16:28:12	1641
NGC 4390	12:25:50.7	10:27:32	1131
NGC 4394	12:25:55.7	18:12:50	862
NGC 4423	12:27:09.0	05:52:49	1104
IC 3365	12:27:11.6	15:53:46	2375
NGC 4430	12:27:26.2	06:15:46	1468
UGC 07590	12:28:18.8	08:43:46	1118
NGC 4468	12:29:30.9	14:02:57	908
NGC 4470	12:29:37.8	07:49:23	2366
NGC 4522	12:33:39.7	09:10:26	2342
NGC 4532	12:34:19.5	06:28:02	2052
UGC 07739	12:34:45.0	06:18:06	1997
IC 3522	12:34:45.9	15:13:13	668
NGC 4561	12:36:08.2	19:19:21	1430
NGC 4567	12:36:32.8	11:15:28	2227
NGC 4568	12:36:34.3	11:14:19	2256
IC 3583	12:36:43.7	13:15:32	1039
IC 3591	12:37:02.6	06:55:33	1635
IC 3617	12:39:24.7	07:57:52	2079
NGC 4595	12:39:51.9	15:17:52	604
NGC 4639	12:42:52.5	13:15:23	977
NGC 4640	12:42:57.8	12:17:12	2082
NGC 4647	12:43:32.6	11:34:57	1334
NGC 4651	12:43:42.7	16:23:36	804

[a]From RC3 (de Vaucouleurs et al. 1991).
[b]Systemic velocity from the H I line (heliocentric).

APPENDIX B: EFFECT OF SHARED OFFS ON CALCULATING UNCERTAINTY FOR $L_{\rm CO(3-2)}$

Both the jiggle and raster mapping modes used in this survey make use of a shared 'off' position in order to increase the mapping efficiency. For the jiggle observations, the off position is observed after each complete cycle through the 16 different pointings that produce a complete map. For a raster observation, the off position is observed after the completion of a scan of a single row. The result of using a shared off is that the noise is somewhat correlated between different pixels in the map because the same off position is used for many 'on' observations. While the noise is estimated properly for any individual pixel in the map, summing many pixels to obtain the total luminosity of an extended object requires a careful estimate of the resulting uncertainty. In effect, if σ_i is the measurement uncertainty in a single pixel, then $\sqrt{\sum \sigma_i^2}$ will underestimate the uncertainty in the summed luminosity because of the effect of the shared offs.

Consider first a very simple situation where we have n ONs all sharing the same single OFF measurement. If we average n ONs, the uncertainty in that average is given by

$$\sigma_{\rm ON,avg} = \sqrt{\sum_{i=1}^{n} \sigma_{{\rm ON},i}^2}/n.$$

But since the OFF is identical for all measurements, we have $\sigma_{\rm OFF,avg} = \sigma_{\rm OFF}$ and the uncertainty in the average difference ON–OFF is given by

$$\sigma_{\rm ON-OFF,avg} = \sqrt{\sum_{i=1}^{n} \sigma_{{\rm ON},i}^2/n^2 + \sigma_{{\rm OFF},j}^2}.$$

We can rewrite this equation as

$$n\sigma_{\rm ON-OFF,avg} = \sqrt{\sum_{i=1}^{n} \sigma_{{\rm ON},i}^2 + n^2\sigma_{{\rm OFF},j}^2} \quad \text{(B1)}$$

to arrive at an expression for $\sigma_L = n\sigma_{\rm ON-OFF,avg}$, the uncertainty in the sum of these n pixels.

We now derive the appropriate formula for the uncertainty in the presence of shared offs where not every pixel has the same off. Suppose we are summing N measurements, where each measurement can be represented as the difference between an ON measurement and an OFF measurement (modulo scaling factors such as system temperature and so on). So then the luminosity can be represented by

$$L = \sum_{i=1}^{N} {\rm ON}_i - \sum_{j=1}^{M} N_j {\rm OFF}_j,$$

where there are N ONs, M OFFs and $\sum_{j=1}^{M} N_j = N$. Let the uncertainty in ON$_i$ be $\sigma_{{\rm ON},i}$ and the uncertainty in OFF$_j$ be $\sigma_{{\rm OFF},j}$. The uncertainty in L, σ_L, is then given by

$$\sigma_L^2 = \sum_{i=1}^{N} \sigma_{{\rm ON},i}^2 + \sum_{j=1}^{M} (N_j\sigma_{{\rm OFF},j})^2. \quad \text{(B2)}$$

It is convenient to define $(N\overline{\sigma}_{\rm OFF})^2 = \sum_{j=1}^{M} (N_j\sigma_{{\rm OFF},j})^2$ so that

$$\sigma_L^2 = \sum_{i=1}^{N} \sigma_{{\rm ON},i}^2 + (N\overline{\sigma}_{\rm OFF})^2.$$

Now, we do not have access to the separate ON and OFF measurements, merely the difference which gives us the signal in each individual pixel. So we will have to be a little clever in getting at the appropriate uncertainty for the sum of many pixels. The measurement uncertainty in any single pixel is given by $\sigma^2_{\mathrm{meas},i} = \sigma^2_{\mathrm{ON},i} + \sigma^2_{\mathrm{OFF},j}$ and so

$$\sum_{i=1}^{N} \sigma^2_{\mathrm{meas},i} = \sum_{i=1}^{N} \sigma^2_{\mathrm{ON},i} + \sum_{j=1}^{M} N_j \sigma^2_{\mathrm{OFF},j}.$$

Now it is easy to show that

$$\sigma_L^2 = \sum_{i=1}^{N} \sigma^2_{\mathrm{meas},i} - \sum_{j=1}^{M} N_j \sigma^2_{\mathrm{OFF},j} + (N\overline{\sigma}_{\mathrm{OFF}})^2. \quad \text{(B3)}$$

Now, for a given receptor in the detector array, $\sigma^2_{\mathrm{OFF},j} = a\overline{\sigma^2_{\mathrm{meas}}} = a\sum_{j=1}^{N_j} \sigma^2_{\mathrm{meas},j}/N_j$, where $a = 1/(t_{\mathrm{off}}/t_{\mathrm{on}} + 1)$ and t_{off} and t_{on} are the integration times spent on the OFF and ON positions, respectively. Similarly, $\sigma_{\mathrm{OFF},j} = \sqrt{a}\sum_{j=1}^{N_j} \sigma_{\mathrm{meas},j}/N_j$ and we can write equation (B3) as

$$\sigma_L^2 = \sum_{i=1}^{N} \sigma^2_{\mathrm{meas},i} - a\sum_{i=1}^{N} \sigma^2_{\mathrm{meas},i} + a\left(\sum_{i=1}^{N} \sigma_{\mathrm{meas},i}\right)^2$$

and we arrive at our final equation for the uncertainty in the sum of N pixels in the presence of shared offs,

$$\sigma_L^2 = (1-a)\sum_{i=1}^{N} \sigma^2_{\mathrm{meas},i} + a\left(\sum_{i=1}^{N} \sigma_{\mathrm{meas},i}\right)^2.$$

For the jiggle-map mode, $t_{\mathrm{off}} = 4t_{\mathrm{on}}$ and so $a = 0.2$. For the raster maps, the ratio of $t_{\mathrm{off}}/t_{\mathrm{on}}$ varied with the size and dimensions of the map; we have estimated an average value of $a = 1.07$ for the rasters and have used this in the noise calculations for all the galaxies.

APPENDIX C: IMAGES OF THE SINGS GALAXIES FROM THE NGLS

In this appendix, we present the images derived from the CO $J = 3-2$ observations of the NGLS galaxies that are also members of the SINGS sample (Kennicutt et al. 2003). Only galaxies with significant detections are shown here; upper limits to the CO luminosity for the remaining galaxies are given in Table 3.

Two images are shown for each galaxy: the CO $J = 3-2$ integrated intensity image, and the CO contours overlaid on an optical image from the Digitized Sky Survey. For those galaxies with sufficient signal-to-noise ratio, we also show the first moment map derived from the CO data cube, which traces the velocity field and the second moment map, which traces the velocity dispersion. The second moment maps for nine galaxies with good signal-to-noise ratio and inclinations less than 60° have been presented and discussed in Wilson et al. (2011) using the same processing techniques used in this paper and so are not reproduced here.

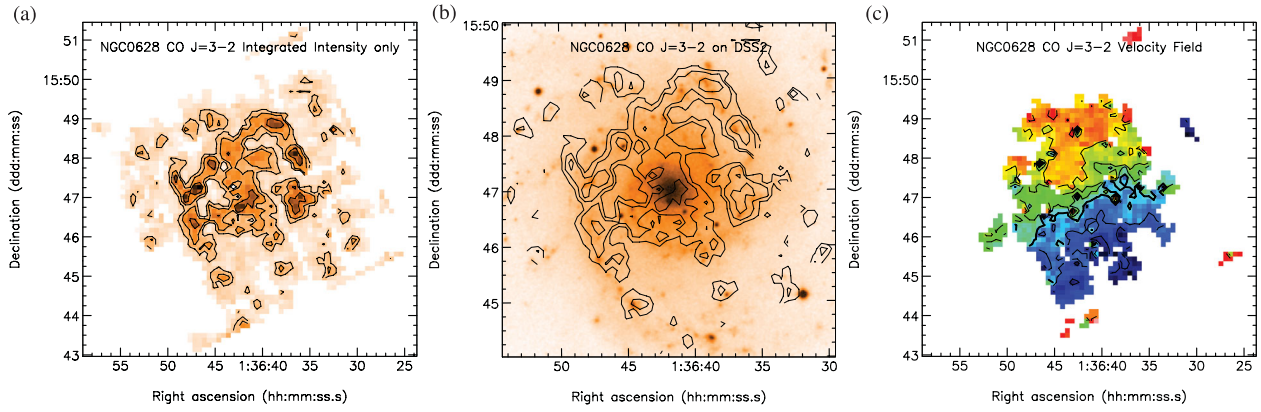

Figure C1. CO $J = 3-2$ images for NGC 0628. (a) CO $J = 3-2$ integrated intensity image. Contours levels are (0.5, 1, 2) K km s^{-1} (T_{MB}). (b) CO $J = 3-2$ integrated intensity contours overlaid on an optical image from the Digitized Sky Survey. (c) Velocity field as traced by the CO $J = 3-2$ first moment map. Contour levels are (624, 632, 640, 648, 656, 664, 672, 680) km s^{-1}. The thick line shows the systemic velocity given in Table 1. Similar images derived from the same data have been published in Warren et al. (2010). The velocity dispersion map has been published in Wilson et al. (2011).

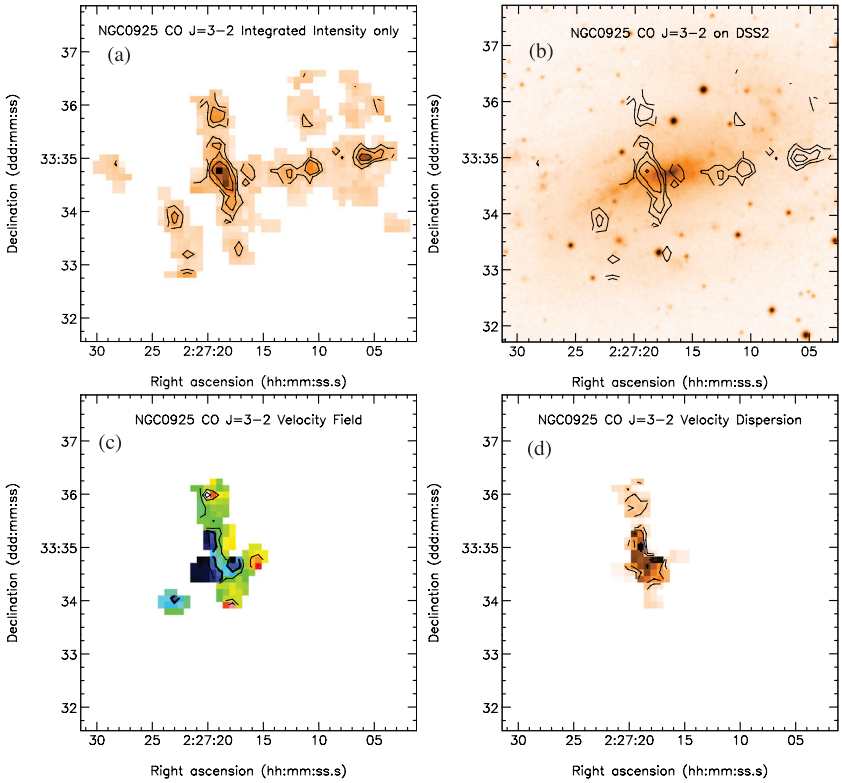

Figure C2. CO $J = 3{-}2$ images for NGC 0925. (a) CO $J = 3{-}2$ integrated intensity image. Contours levels are (0.5, 1, 2, 4) K km s^{-1} ($T_{\rm MB}$). (b) CO $J = 3{-}2$ overlaid on a Digitized Sky Survey image. (c) Velocity field. Contour levels are (525, 540, 555, 570, 585) km s^{-1}. (d) The velocity dispersion $\sigma_{\rm v}$ as traced by the CO $J = 3{-}2$ second moment map. Contour levels are (4, 8, 16) km s^{-1}.

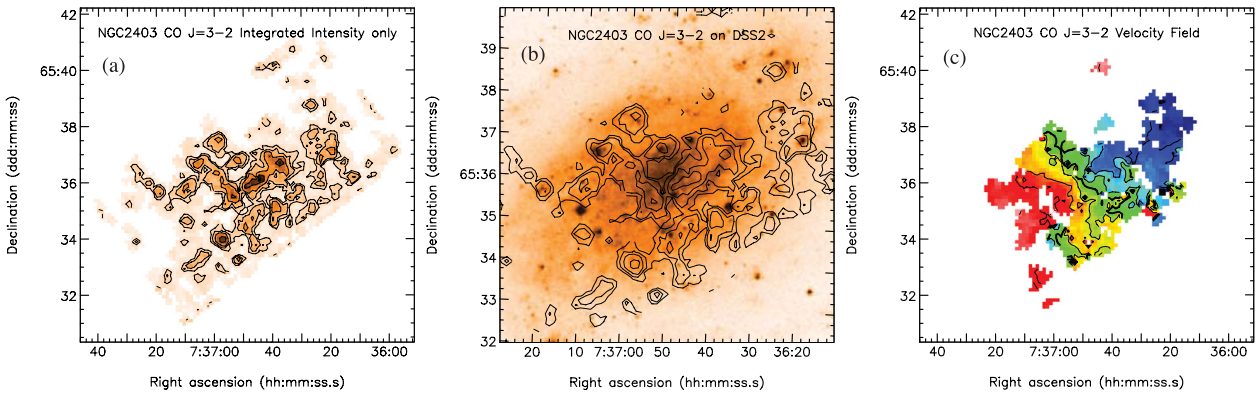

Figure C3. CO $J = 3{-}2$ images for NGC 2403. (a) CO $J = 3{-}2$ integrated intensity image. Contours levels are (0.5, 1, 2, 4) K km s^{-1} ($T_{\rm MB}$). (b) CO $J = 3{-}2$ integrated intensity contours overlaid on an optical image from the Digitized Sky Survey. (c) Velocity field as traced by the CO $J = 3{-}2$ first moment map. Contour levels are (21, 46, 71, 96, 121, 146, 171, 196, 221) km s^{-1}. The velocity dispersion map has been published in Wilson et al. (2011).

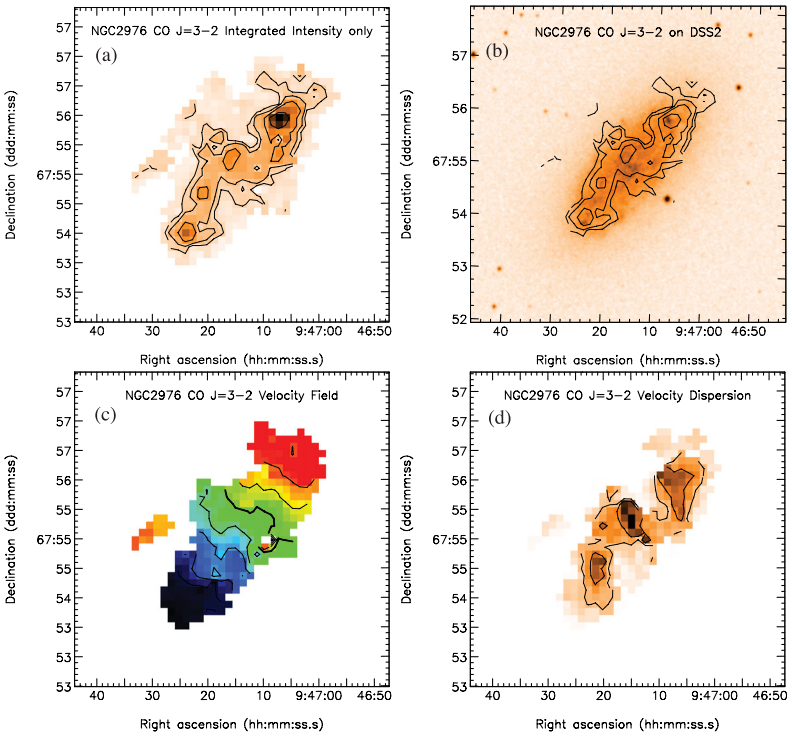

Figure C4. CO $J = 3{-}2$ images for NGC 2976. (a) CO $J = 3{-}2$ integrated intensity image. Contours levels are (0.5, 1, 2, 4) K km s^{-1} (T_{MB}). (b) CO $J = 3{-}2$ overlaid on a Digitized Sky Survey image. (c) Velocity field. Contour levels are (−50, −32, −14, 4, 22, 40, 58, 76, 94) km s^{-1}. (d) The velocity dispersion σ_v as traced by the CO $J = 3{-}2$ second moment map. Contour levels are (4, 8) km s^{-1}.

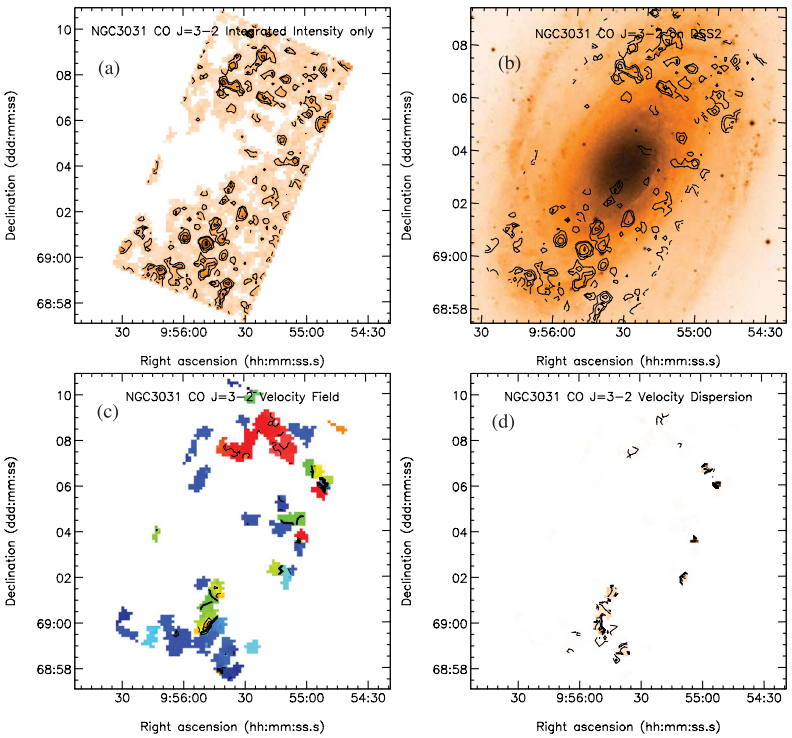

Figure C5. CO $J = 3{-}2$ images for NGC 3031. (a) CO $J = 3{-}2$ integrated intensity image. Contours levels are (0.5, 1, 2, 4) K km s^{-1} (T_{MB}). (b) CO $J = 3{-}2$ overlaid on a Digitized Sky Survey image. (c) Velocity field. Contour levels are (−328, −258, −188, −118, −48, 22, 92, 162) km s^{-1}. (d) The velocity dispersion σ_v as traced by the CO $J = 3{-}2$ second moment map. Contour levels are (4, 8, 16, 32, 64, 128) km s^{-1}. Images derived from the same data using careful flagging and analysis to detect weak but real features have been published in Sanchez-Gallego et al. (2011).

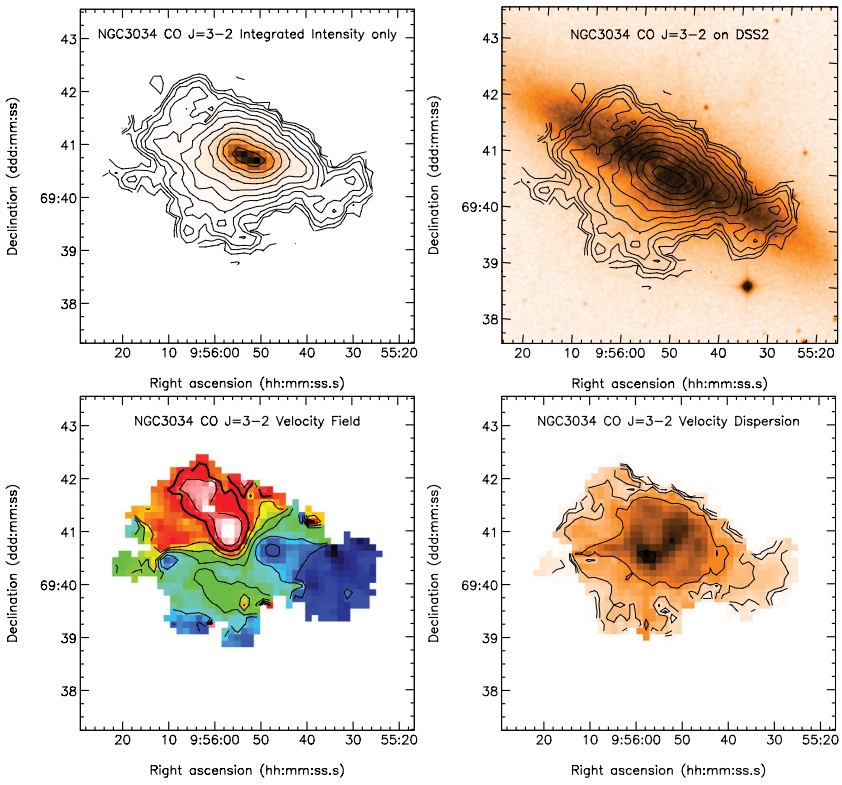

Figure C6. CO $J = 3{-}2$ images for NGC 3034. (a) CO $J = 3{-}2$ integrated intensity image. Contours levels are (0.5, 1, 2, 4, 8, 16, 32, 64, 128, 256, 512) K km s^{-1} ($T_{\rm MB}$). (b) CO $J = 3{-}2$ overlaid on a Digitized Sky Survey image. (c) Velocity field. Contour levels are (129, 154, 179, 204, 229, 254, 279) km s^{-1}. (d) The velocity dispersion $\sigma_{\rm v}$ as traced by the CO $J = 3{-}2$ second moment map. Contour levels are (4, 8, 16, 32, 64) km s^{-1}.

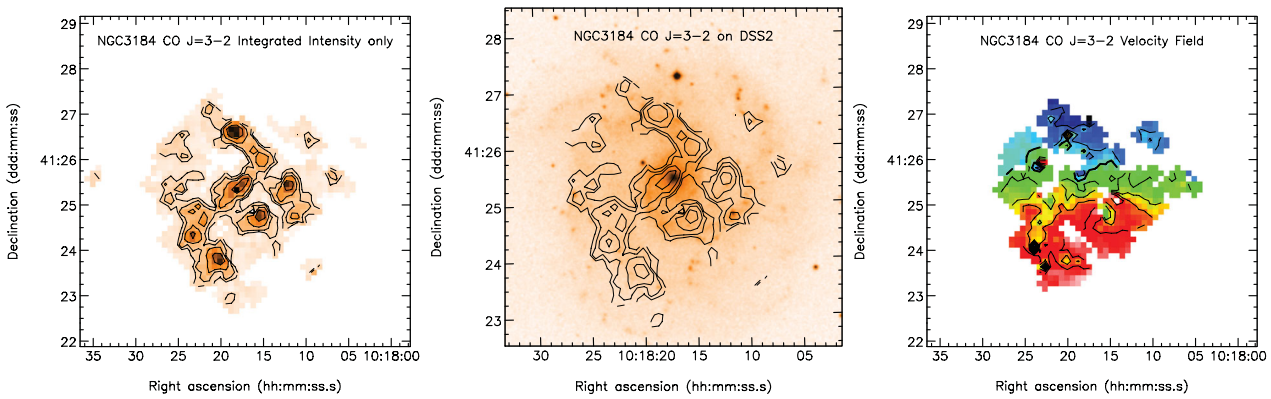

Figure C7. CO $J = 3{-}2$ images for NGC 3184. (a) CO $J = 3{-}2$ integrated intensity image. Contours levels are (0.5, 1, 2, 4) K km s^{-1} ($T_{\rm MB}$). (b) CO $J = 3{-}2$ integrated intensity contours overlaid on an optical image from the Digitized Sky Survey. (c) Velocity field as traced by the CO $J = 3{-}2$ first moment map. Contour levels are (532, 546, 560, 574, 588, 602, 616, 630) km s^{-1}. The velocity dispersion map has been published in Wilson et al. (2011).

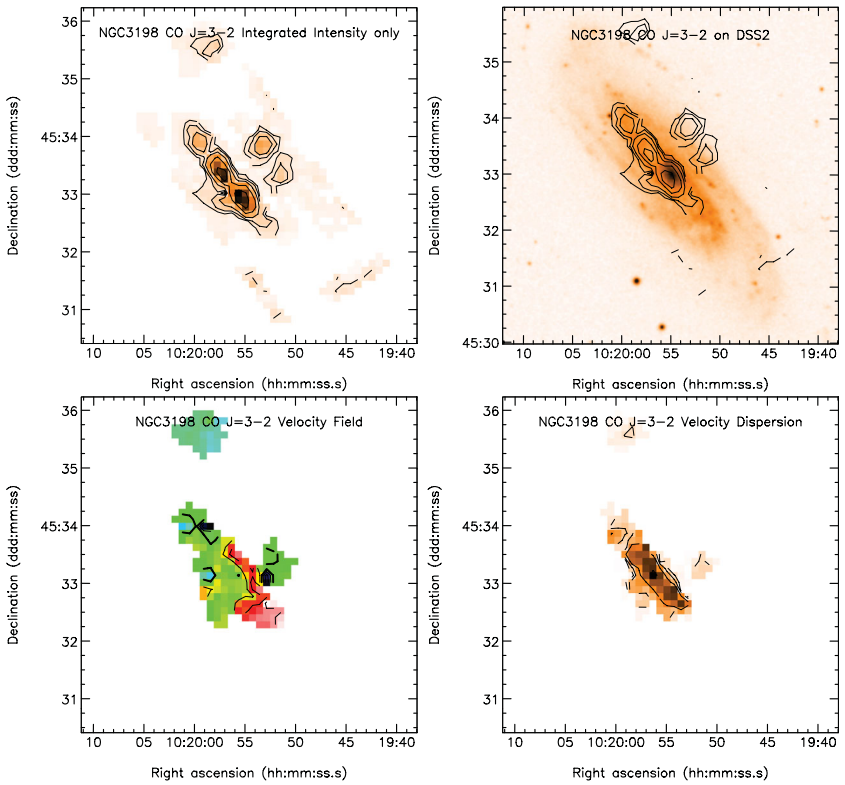

Figure C8. CO $J = 3-2$ images for NGC 3198. (a) CO $J = 3-2$ integrated intensity image. Contours levels are (0.5, 1, 2, 4, 8) K km s^{-1} (T_{MB}). (b) CO $J = 3-2$ overlaid on a Digitized Sky Survey image. (c) Velocity field. Contour levels are (606, 636, 666, 696, 726, 756) km s^{-1}. (d) The velocity dispersion σ_v as traced by the CO $J = 3-2$ second moment map. Contour levels are (4, 8, 16, 32) km s^{-1}.

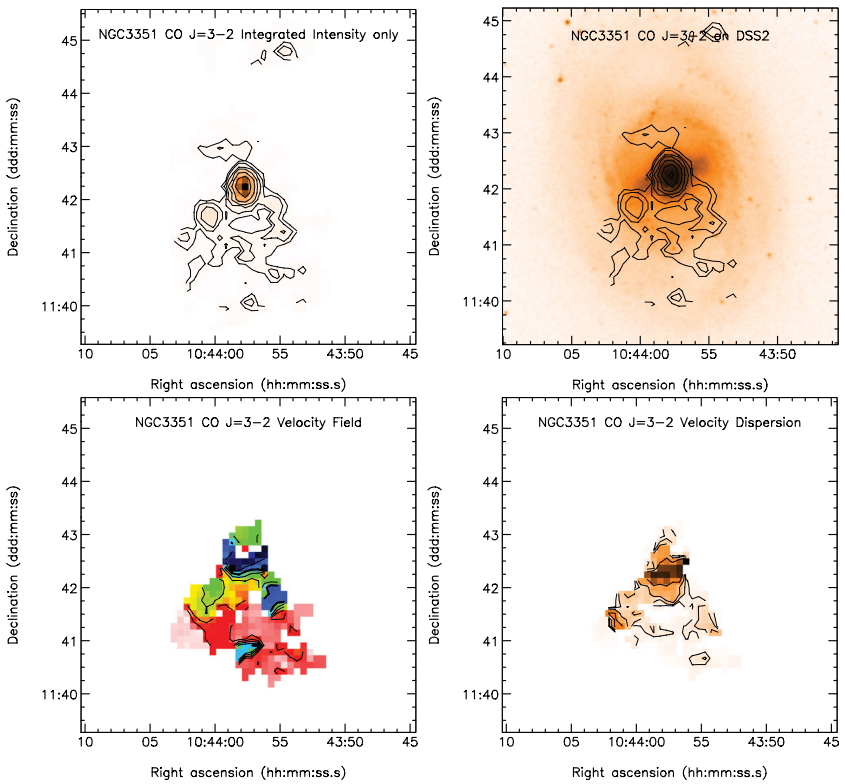

Figure C9. CO $J = 3-2$ images for NGC 3351. (a) CO $J = 3-2$ integrated intensity image. Contours levels are (0.5, 1, 2, 4, 8, 16, 32) K km s^{-1} (T_{MB}). (b) CO $J = 3-2$ overlaid on a Digitized Sky Survey image. (c) Velocity field. Contour levels are (702, 735, 768, 801, 834, 867, 900) km s^{-1}. (d) The velocity dispersion σ_v as traced by the CO $J = 3-2$ second moment map. Contour levels are (4, 8, 16, 32, 64) km s^{-1}.

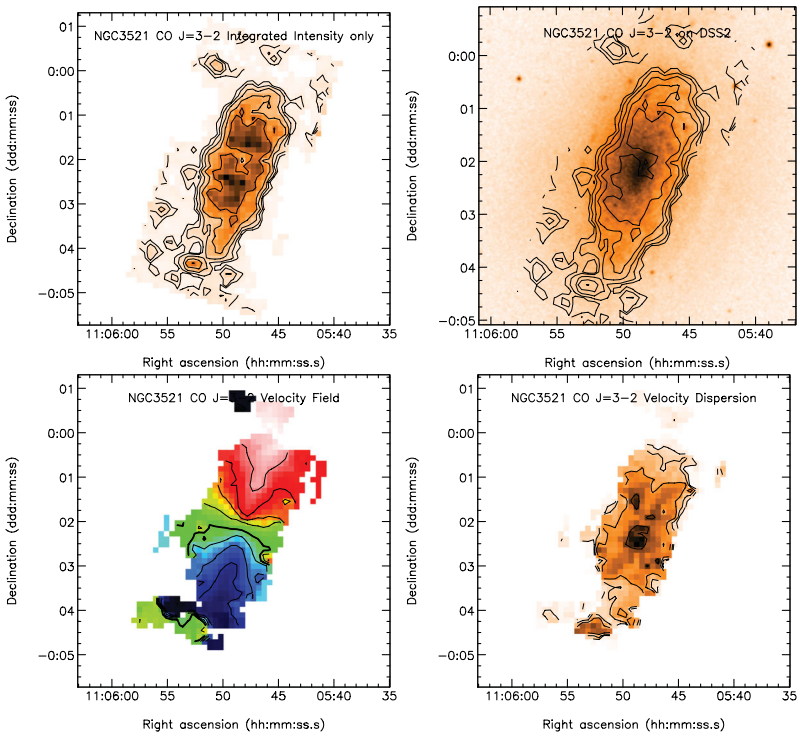

Figure C10. CO $J = 3{-}2$ images for NGC 3521. (a) CO $J = 3{-}2$ integrated intensity image. Contours levels are (0.5, 1, 2, 4, 8) K km s^{-1} ($T_{\rm MB}$). (b) CO $J = 3{-}2$ overlaid on a Digitized Sky Survey image. (c) Velocity field. Contour levels are (558, 613, 668, 723, 778, 833, 888, 943, 998) km s^{-1}. (d) The velocity dispersion $\sigma_{\rm v}$ as traced by the CO $J = 3{-}2$ second moment map. Contour levels are (4, 8, 16, 32) km s^{-1}. Similar images derived from the same data have been published in Warren et al. (2010).

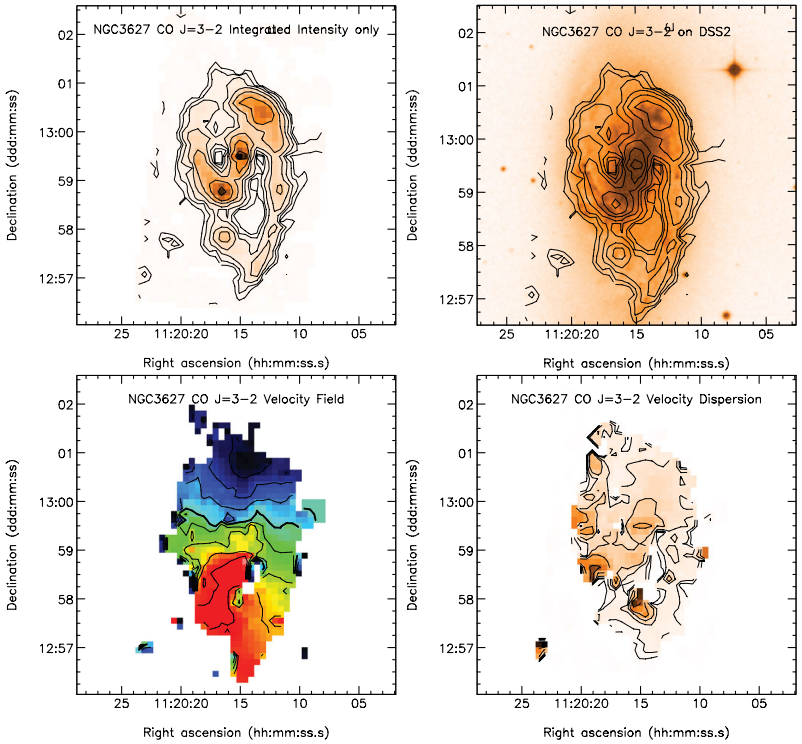

Figure C11. CO $J = 3{-}2$ images for NGC 3627. (a) CO $J = 3{-}2$ integrated intensity image. Contours levels are (0.5, 1, 2, 4, 8, 16, 32) K km s^{-1} ($T_{\rm MB}$). (b) CO $J = 3{-}2$ overlaid on a Digitized Sky Survey image. (c) Velocity field. Contour levels are (559, 605, 651, 697, 743, 789, 835, 881) km s^{-1}. (d) The velocity dispersion $\sigma_{\rm v}$ as traced by the CO $J = 3{-}2$ second moment map. Contour levels are (4, 8, 16, 32, 64, 128) km s^{-1}. Similar images derived from the same data have been published in Warren et al. (2010).

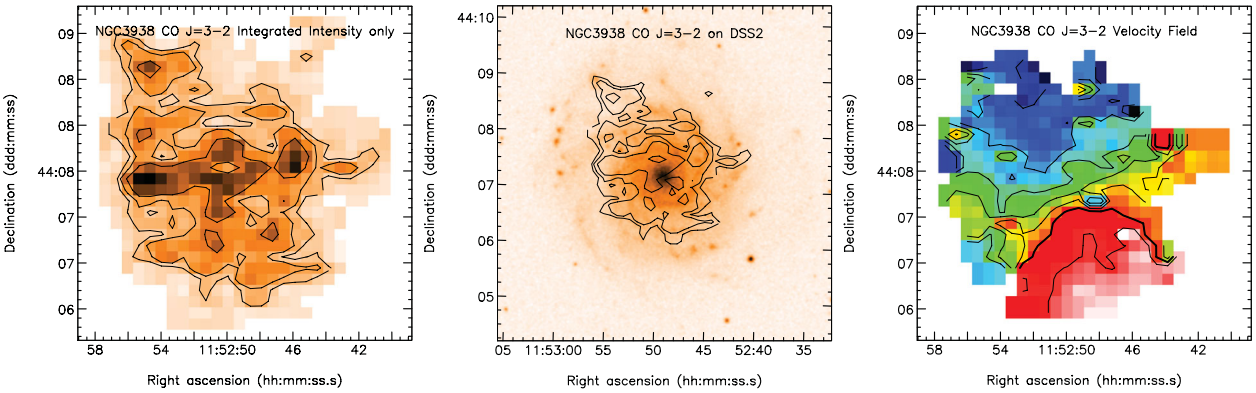

Figure C12. CO $J = 3{-}2$ images for NGC 3938. (a) CO $J = 3{-}2$ integrated intensity image. Contours levels are (0.5, 1, 2) K km s^{-1} (T_{MB}). (b) CO $J = 3{-}2$ integrated intensity contours overlaid on an optical image from the Digitized Sky Survey. (c) Velocity field as traced by the CO $J = 3{-}2$ first moment map. Contour levels are (769, 781, 793, 805, 817, 829, 841) km s^{-1}. The velocity dispersion map has been published in Wilson et al. (2011).

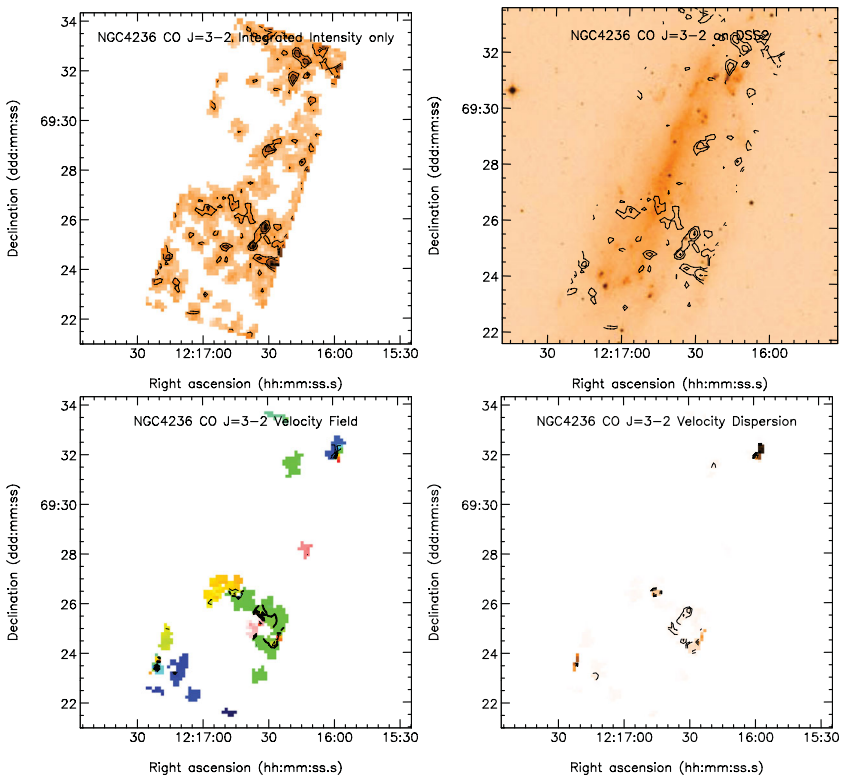

Figure C13. CO $J = 3{-}2$ images for NGC 4236. (a) CO $J = 3{-}2$ integrated intensity image. Contours levels are (0.5, 1, 2) K km s^{-1} (T_{MB}). (b) CO $J = 3{-}2$ overlaid on a Digitized Sky Survey image. (c) Velocity field. Contour levels are (−190, −150, −110, −70, −30, 10, 50, 90, 130, 170) km s^{-1}. (d) The velocity dispersion σ_v as traced by the CO $J = 3{-}2$ second moment map. Contour levels are (4, 8, 16, 32, 64) km s^{-1}.

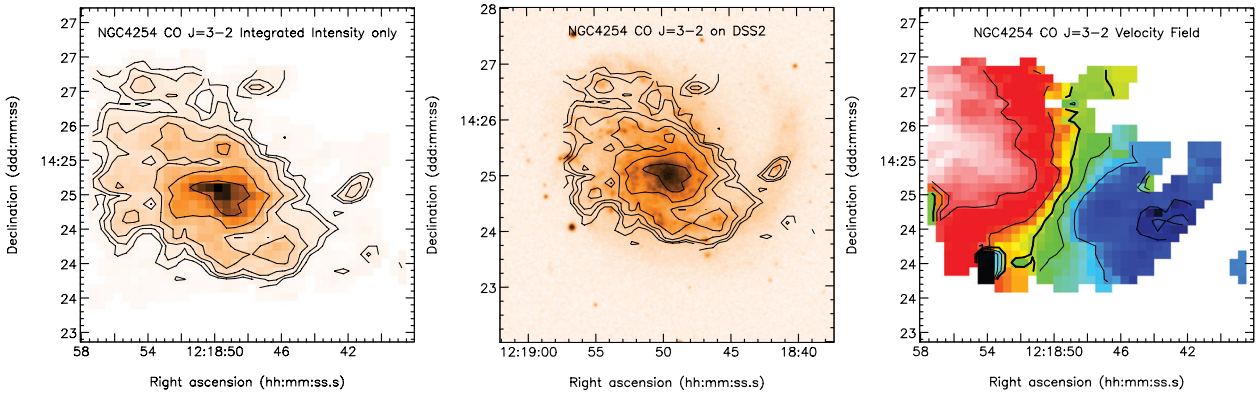

Figure C14. CO $J = 3{-}2$ images for NGC 4254. (a) CO $J = 3{-}2$ integrated intensity image. Contours levels are (0.5, 1, 2, 4, 8, 16) K km s^{-1} ($T_{\rm MB}$). (b) CO $J = 3{-}2$ integrated intensity contours overlaid on an optical image from the Digitized Sky Survey. (c) Velocity field as traced by the CO $J = 3{-}2$ first moment map. Contour levels are (2304, 2340, 2376, 2412, 2448, 2484) km s^{-1}. Similar images derived from the same data have been published in Wilson et al. (2009). The velocity dispersion map has been published in Wilson et al. (2011).

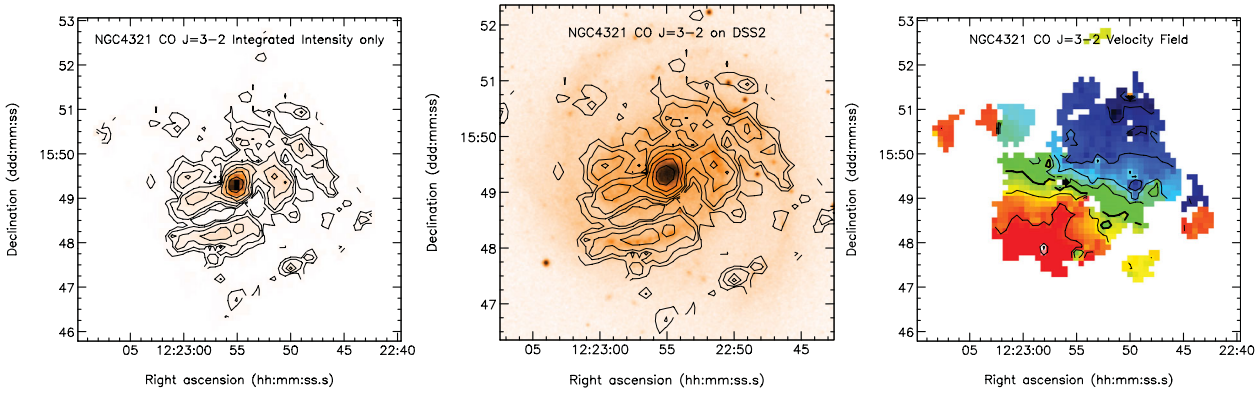

Figure C15. CO $J = 3{-}2$ images for NGC 4321. (a) CO $J = 3{-}2$ integrated intensity image. Contours levels are (0.5, 1, 2, 4, 8, 16, 32) K km s^{-1} ($T_{\rm MB}$). (b) CO $J = 3{-}2$ integrated intensity contours overlaid on an optical image from the Digitized Sky Survey. (c) Velocity field as traced by the CO $J = 3{-}2$ first moment map. Contour levels are (1424, 1459, 1494, 1529, 1564, 1599, 1634, 1669, 1704, 1739) km s^{-1}. Similar images derived from the same data have been published in Wilson et al. (2009). The velocity dispersion map has been published in Wilson et al. (2011).

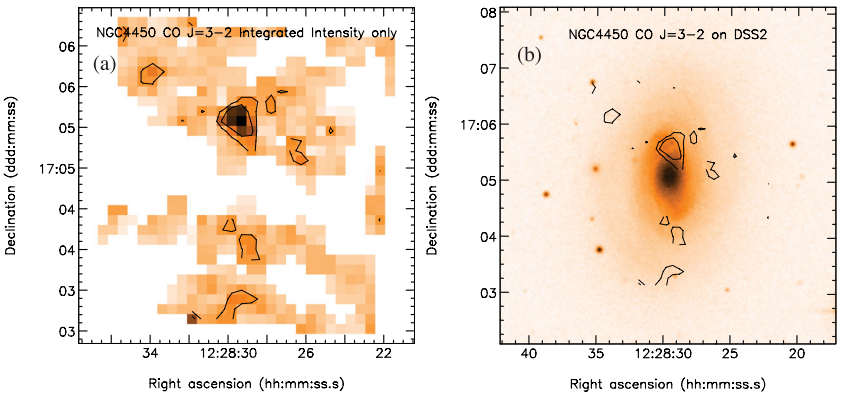

Figure C16. CO $J = 3{-}2$ images for NGC 4450. (a) CO $J = 3{-}2$ integrated intensity image. Contours levels are (0.5, 1) K km s^{-1} ($T_{\rm MB}$). (b) CO $J = 3{-}2$ overlaid on a Digitized Sky Survey image.

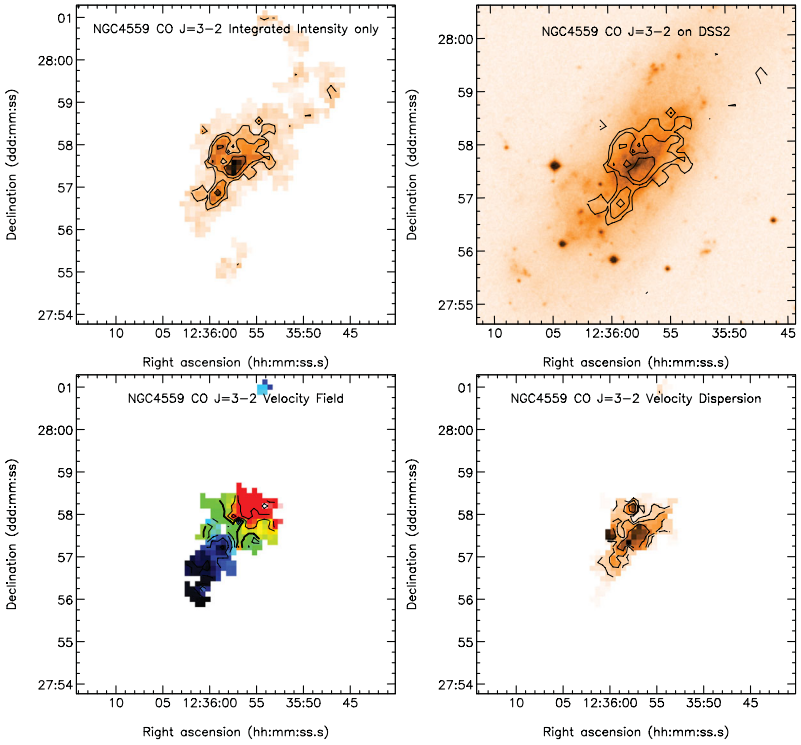

Figure C17. CO $J = 3-2$ images for NGC 4559. (a) CO $J = 3-2$ integrated intensity image. Contours levels are (0.5, 1, 2) K km s^{-1} (T_{MB}). (b) CO $J = 3-2$ overlaid on a Digitized Sky Survey image. (c) Velocity field. Contour levels are (735, 758, 781, 804, 827, 850, 873, 896) km s^{-1}. (d) The velocity dispersion σ_v as traced by the CO $J = 3-2$ second moment map. Contour levels are (4, 8, 16) km s^{-1}.

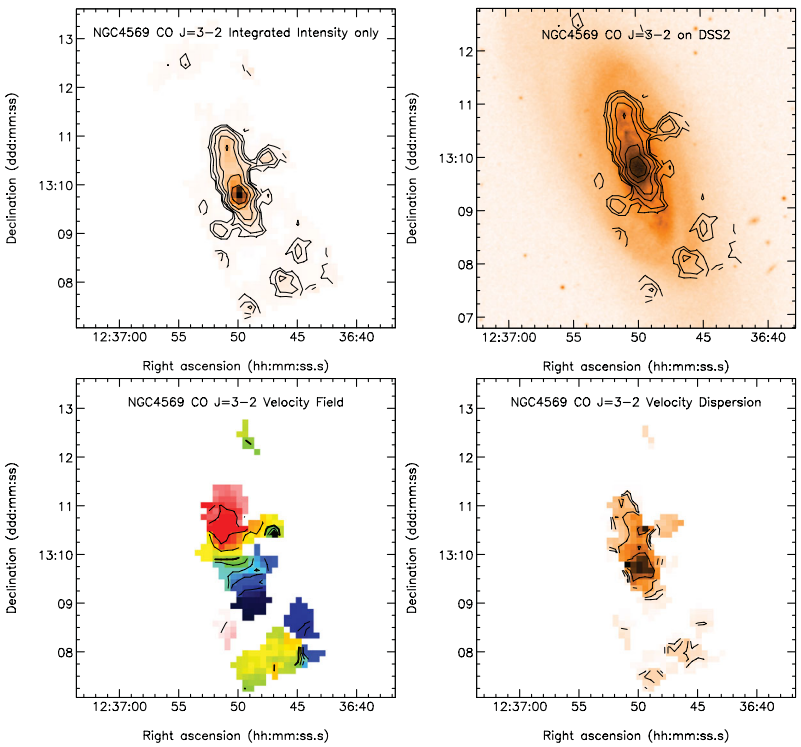

Figure C18. CO $J = 3-2$ images for NGC 4569. (a) CO $J = 3-2$ integrated intensity image. Contours levels are (0.5, 1, 2, 4, 8, 16) K km s^{-1} (T_{MB}). (b) CO $J = 3-2$ overlaid on a Digitized Sky Survey image. (c) Velocity field. Contour levels are (−379, −339, −299, −259, −219, −179, −139, −99, −59, −19) km s^{-1}. (d) The velocity dispersion σ_v as traced by the CO $J = 3-2$ second moment map. Contour levels are (4, 8, 16, 32) km s^{-1}. Similar images derived from the same data have been published in Wilson et al. (2009).

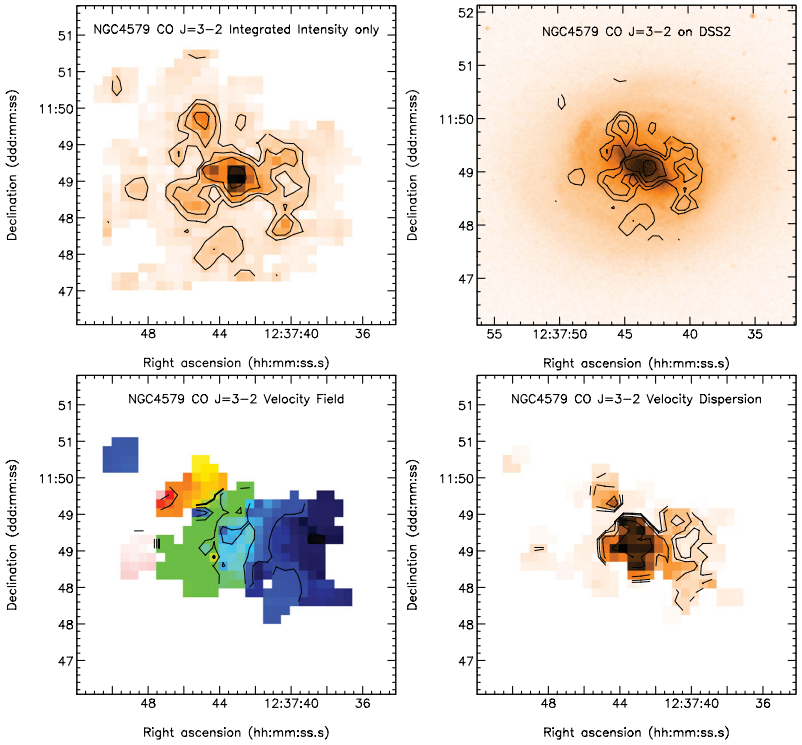

Figure C19. CO $J = 3{-}2$ images for NGC 4579. (a) CO $J = 3{-}2$ integrated intensity image. Contours levels are (0.5, 1, 2, 4) K km s^{-1} ($T_{\rm MB}$). (b) CO $J = 3{-}2$ overlaid on a Digitized Sky Survey image. (c) Velocity field. Contour levels are (1340, 1390, 1440, 1490, 1540, 1590, 1640, 1690) km s^{-1}. (d) The velocity dispersion $\sigma_{\rm v}$ as traced by the CO $J = 3{-}2$ second moment map. Contour levels are (4, 8, 16, 32) km s^{-1}. Images of this galaxy derived from early observations in the survey have been published in Wilson et al. (2009). These images are made using later data which had a higher quality.

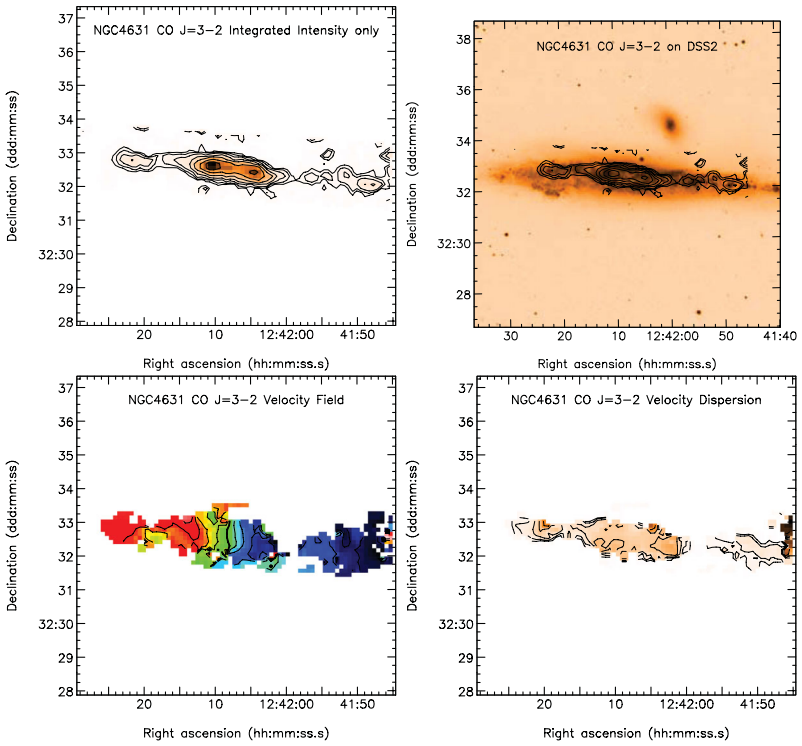

Figure C20. CO $J = 3{-}2$ images for NGC 4631. (a) CO $J = 3{-}2$ integrated intensity image. Contours levels are (0.5, 1, 2, 4, 8, 16, 32) K km s^{-1} ($T_{\rm MB}$). (b) CO $J = 3{-}2$ overlaid on a Digitized Sky Survey image. (c) Velocity field. Contour levels are (520, 550, 580, 610, 640, 670, 700, 730, 760) km s^{-1}. (d) The velocity dispersion $\sigma_{\rm v}$ as traced by the CO $J = 3{-}2$ second moment map. Contour levels are (4, 8, 16, 32, 64, 128) km s^{-1}. Similar images derived from the same data have been published in Irwin et al. (2011).

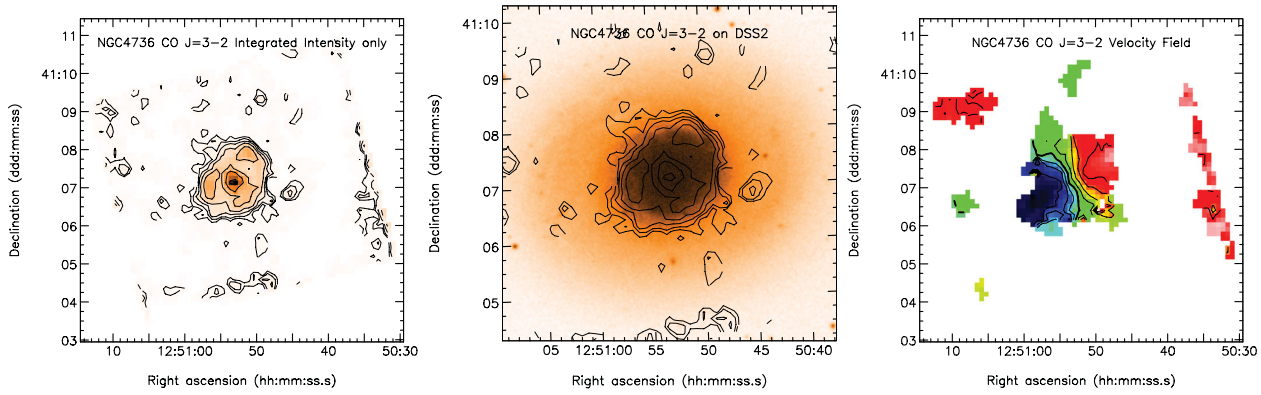

Figure C21. CO $J = 3{-}2$ images for NGC 4736. (a) CO $J = 3{-}2$ integrated intensity image. Contours levels are (0.5, 1, 2, 4, 8, 16, 32) K km s^{-1} (T_{MB}). (b) CO $J = 3{-}2$ integrated intensity contours overlaid on an optical image from the Digitized Sky Survey. (c) Velocity field as traced by the CO $J = 3{-}2$ first moment map. Contour levels are (214, 241, 268, 295, 322, 349, 376, 403) km s^{-1}. The velocity dispersion map has been published in Wilson et al. (2011).

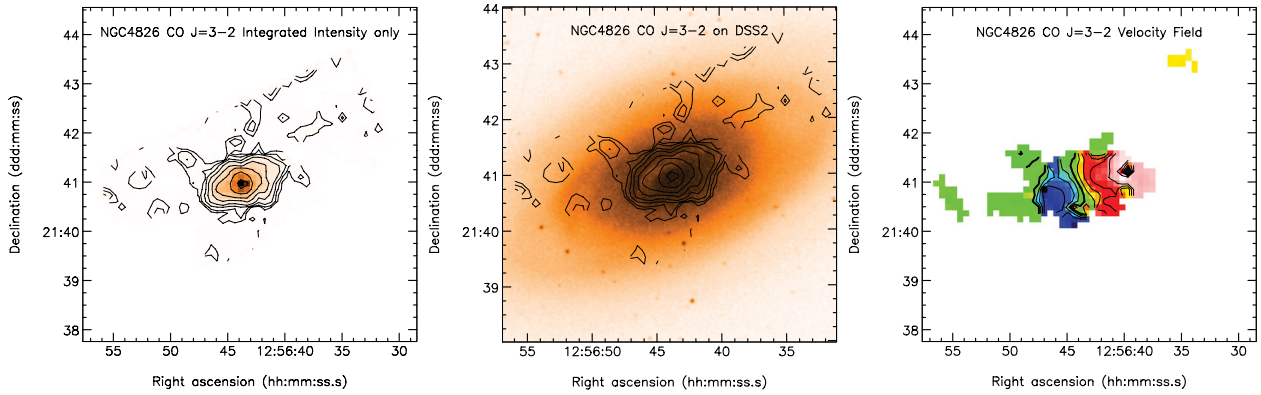

Figure C22. CO $J = 3{-}2$ images for NGC 4826. (a) CO $J = 3{-}2$ integrated intensity image. Contours levels are (0.5, 1, 2, 4, 8, 16, 32, 64) K km s^{-1} (T_{MB}). (b) CO $J = 3{-}2$ integrated intensity contours overlaid on an optical image from the Digitized Sky Survey. (c) Velocity field as traced by the CO $J = 3{-}2$ first moment map. Contour levels are (230, 270, 310, 350, 390, 430, 470, 510, 550) km s^{-1}. The velocity dispersion map has been published in Wilson et al. (2011).

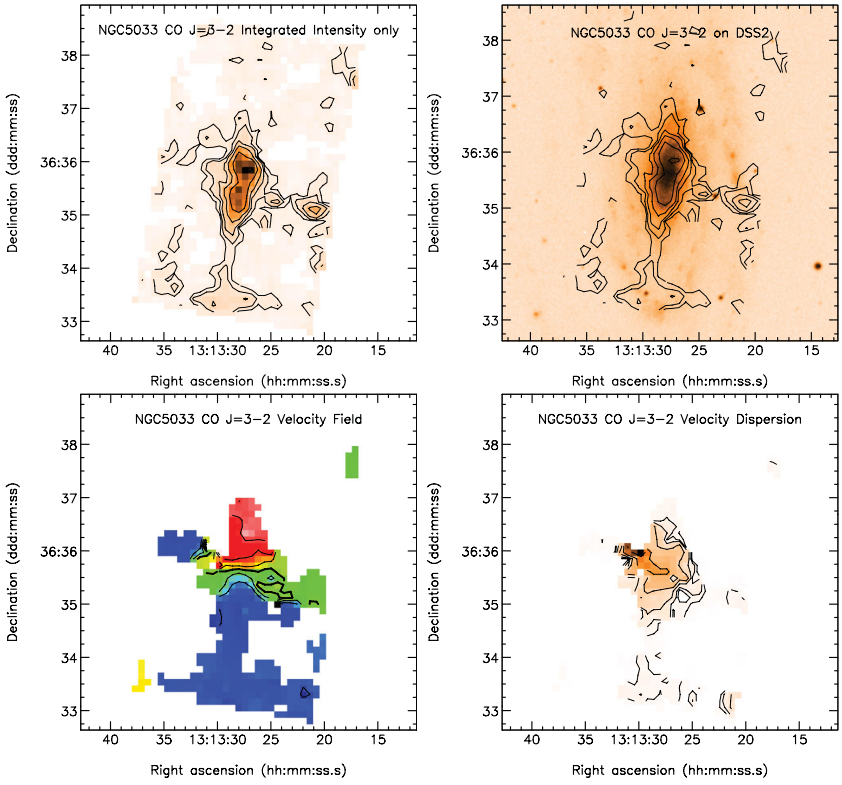

Figure C23. CO $J = 3{-}2$ images for NGC 5033. (a) CO $J = 3{-}2$ integrated intensity image. Contours levels are (0.5, 1, 2, 4, 8, 16) K km s^{-1} ($T_{\rm MB}$). (b) CO $J = 3{-}2$ overlaid on a Digitized Sky Survey image. (c) Velocity field. Contour levels are (593, 663, 733, 803, 873, 943, 1013, 1083) km s^{-1}. (d) The velocity dispersion $\sigma_{\rm v}$ as traced by the CO $J = 3{-}2$ second moment map. Contour levels are (4, 8, 16, 32, 64, 128) km s^{-1}.

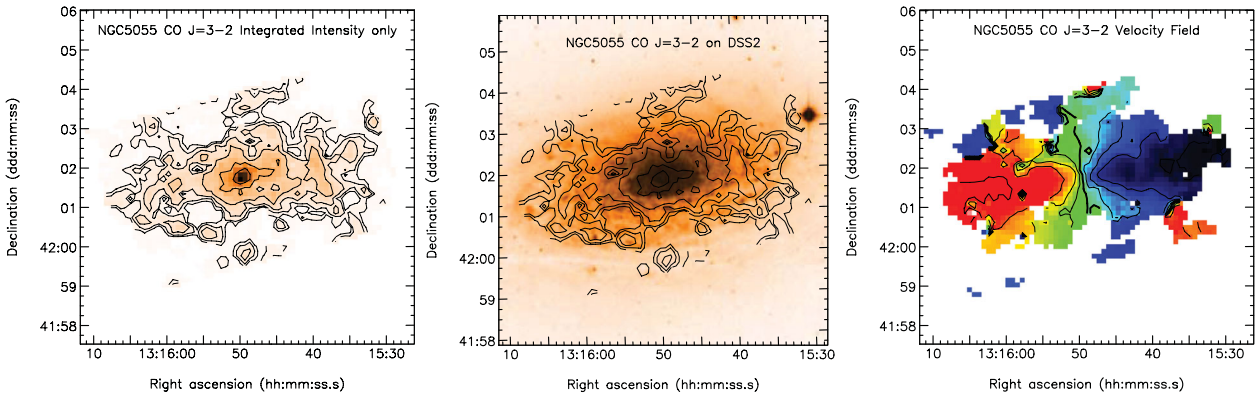

Figure C24. CO $J = 3{-}2$ images for NGC 5055. (a) CO $J = 3{-}2$ integrated intensity image. Contours levels are (0.5, 1, 2, 4, 8, 16) K km s^{-1} ($T_{\rm MB}$). (b) CO $J = 3{-}2$ integrated intensity contours overlaid on an optical image from the Digitized Sky Survey. (c) Velocity field as traced by the CO $J = 3{-}2$ first moment map. Contour levels are (315, 360, 405, 450, 495, 540, 585, 630, 675) km s^{-1}. The velocity dispersion map has been published in Wilson et al. (2011).

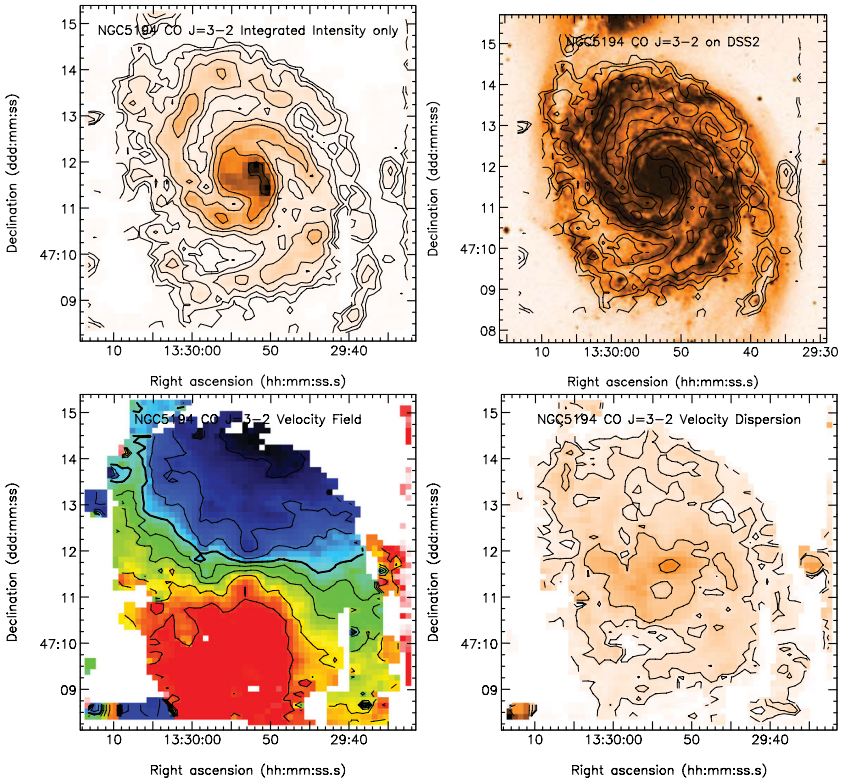

Figure C25. CO $J = 3-2$ images for NGC 5194. (a) CO $J = 3-2$ integrated intensity image. Contours levels are (0.5, 1, 2, 4, 8, 16, 32) K km s^{-1} (T_{MB}). (b) CO $J = 3-2$ overlaid on a Digitized Sky Survey image. (c) Velocity field. Contour levels are (392, 412, 432, 452, 472, 492, 512, 532) km s^{-1}. (d) The velocity dispersion σ_v as traced by the CO $J = 3-2$ second moment map. Contour levels are (4, 8, 16, 32, 64) km s^{-1}. A more complete analysis of the data for NGC 5194 will be published in Vlahakis et al. (in preparation).

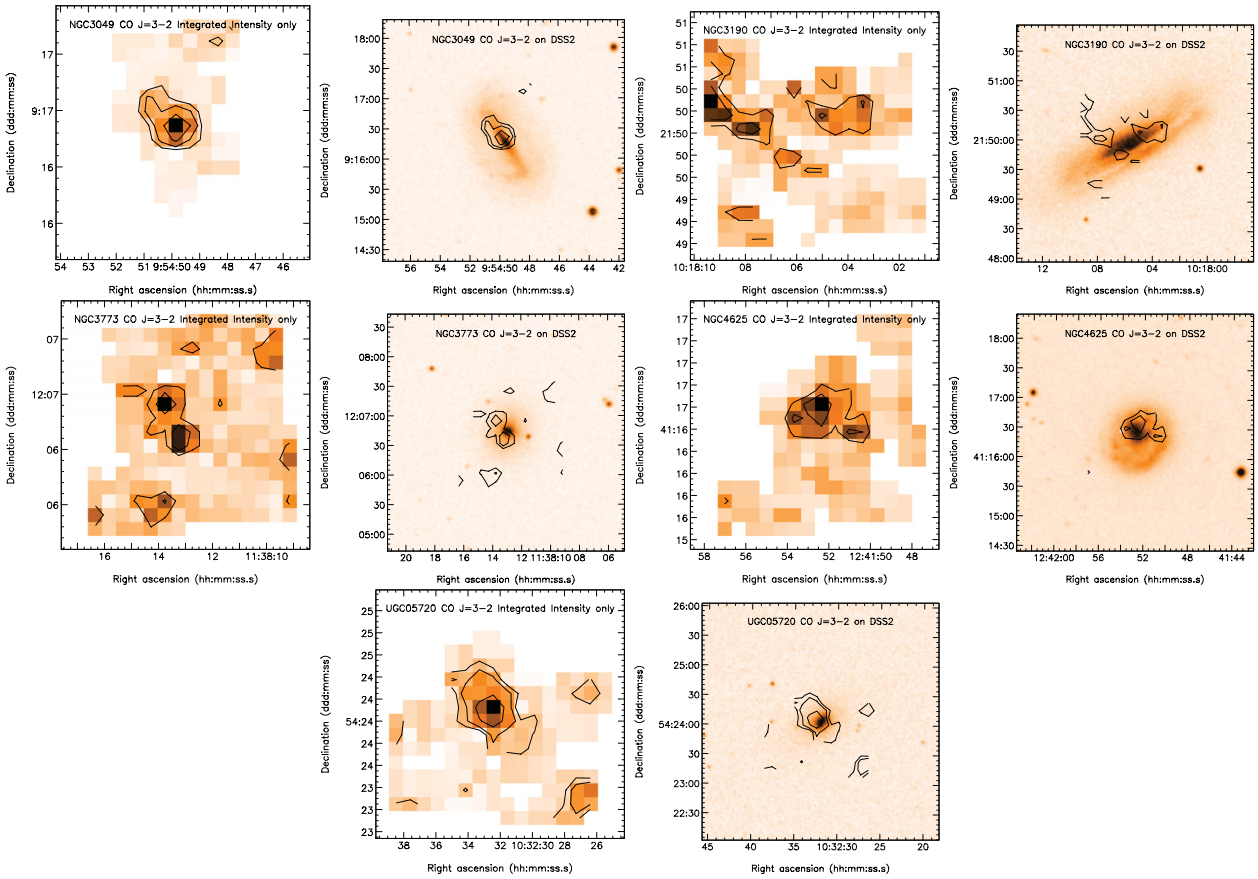

Figure C26. CO $J = 3{-}2$ images for the small SINGS galaxies detected in jiggle-map mode. See Fig. C1 for more details. Left of pair: CO $J = 3{-}2$ integrated intensity image. Contours levels are (0.5, 1, 2, 4) K km s^{-1} ($T_{\rm MB}$). Right of pair: CO $J = 3{-}2$ overlaid on a Digitized Sky Survey image.

This paper has been typeset from a TEX/LATEX file prepared by the author.